



# A conservative Eulerian-Lagrangian decomposition principle for the solution of multi-scale flow problems at high Schmidt or Prandtl numbers

M. Leer, M.W.A. Pettit, J.T. Lipkowicz, Pascale Domingo, L. Vervisch, A.M. Kempf

## ► To cite this version:

M. Leer, M.W.A. Pettit, J.T. Lipkowicz, Pascale Domingo, L. Vervisch, et al.. A conservative Eulerian-Lagrangian decomposition principle for the solution of multi-scale flow problems at high Schmidt or Prandtl numbers. *Journal of Computational Physics*, 2022, 464, pp.111216. 10.1016/j.jcp.2022.111216 . hal-03784194

**HAL Id: hal-03784194**

**<https://normandie-univ.hal.science/hal-03784194>**

Submitted on 22 Sep 2022

**HAL** is a multi-disciplinary open access archive for the deposit and dissemination of scientific research documents, whether they are published or not. The documents may come from teaching and research institutions in France or abroad, or from public or private research centers.

L'archive ouverte pluridisciplinaire **HAL**, est destinée au dépôt et à la diffusion de documents scientifiques de niveau recherche, publiés ou non, émanant des établissements d'enseignement et de recherche français ou étrangers, des laboratoires publics ou privés.

# Journal Pre-proof

A conservative Eulerian-Lagrangian decomposition principle for the solution of multi-scale flow problems at high Schmidt or Prandtl numbers

M. Leer, M.W.A. Pettit, J.T. Lipkowitz, P. Domingo, L. Vervisch et al.

PII: S0021-9991(22)00278-9  
DOI: <https://doi.org/10.1016/j.jcp.2022.111216>  
Reference: YJCPH 111216

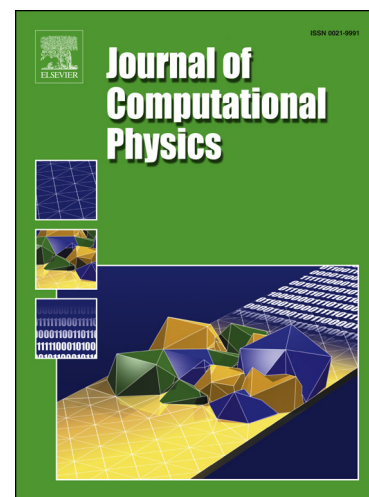
To appear in: *Journal of Computational Physics*

Received date: 12 October 2021  
Revised date: 17 February 2022  
Accepted date: 7 April 2022

Please cite this article as: M. Leer, M.W.A. Pettit, J.T. Lipkowitz et al., A conservative Eulerian-Lagrangian decomposition principle for the solution of multi-scale flow problems at high Schmidt or Prandtl numbers, *Journal of Computational Physics*, 111216, doi: <https://doi.org/10.1016/j.jcp.2022.111216>.

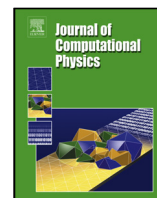
This is a PDF file of an article that has undergone enhancements after acceptance, such as the addition of a cover page and metadata, and formatting for readability, but it is not yet the definitive version of record. This version will undergo additional copyediting, typesetting and review before it is published in its final form, but we are providing this version to give early visibility of the article. Please note that, during the production process, errors may be discovered which could affect the content, and all legal disclaimers that apply to the journal pertain.

© 2022 Published by Elsevier.



**Highlights**

- The transport of scalar quantities at high Schmidt numbers is becoming an increasingly important phenomenon in science.
- Their accurate numerical simulation is extremely costly with the methods and resources that are currently available.
- The development of a joint Euler-Lagrangian concept combining FVM with particle methods is a promising approach provided that the integration is well designed.
- A concentrated use of particles in regions where they provide a substantial gain in resolution ensures high numerical efficiency.



## A conservative Eulerian-Lagrangian decomposition principle for the solution of multi-scale flow problems at high Schmidt or Prandtl numbers

M. Leer<sup>a,\*</sup>, M. W. A. Pettit<sup>b</sup>, J. T. Lipkowitz<sup>a</sup>, P. Domingo<sup>c</sup>, L. Vervisch<sup>c</sup>, A. M. Kempf<sup>a</sup>

<sup>a</sup>Chair of Fluid Dynamics, IVG, Duisburg-Essen University, 47057 Duisburg, Germany

<sup>b</sup>Department of Mechanical Engineering, Imperial College London, SW7 2AZ London, United Kingdom

<sup>c</sup>CORIA – CNRS, Normandie Université, INSA Rouen Normandie, 76801 Saint-Etienne-du-Rouvray, France

### ARTICLE INFO

#### Article history:

Received 1 May 2013

Received in final form 10 May 2013

Accepted 13 May 2013

Available online 15 May 2013

#### Keywords:

Scalar transport

Lagrangian particles

Finite Volume Method

Numerical diffusion

Low-pass filter

Microscale

### ABSTRACT

The simulation of turbulent flow that involves scalar transport at high Schmidt or Prandtl numbers is a major challenge. Enhanced Schmidt and Prandtl numbers demand an excessive increase in numerical resolution. Otherwise, the accuracy of transport would suffer substantially through unresolved information and numerical diffusion. With the aim of providing an efficient alternative for such applications, this paper presents a simulation method that is based on a novel *Eulerian-Lagrangian decomposition principle* (ELD) of the transported quantity. Low-pass filtering of the initial scalar quantity field separates it into a smooth *low-frequency* component and a fine-structured *high-frequency* component. The low-frequency component is represented and transported according to the Eulerian description by applying the Finite Volume Method (FVM) with a numerical resolution according to the Kolmogorov scale. The high-frequency component is translated into the Lagrangian description by the formation of particles, which are transported in parallel. By exchanging information between the two components, a re-initialisation mechanism ensures that the frequency-based decomposition is maintained throughout the simulation. Such ELD approach combines the efficiency of the FVM with the numerical stability of Lagrangian particles. As a result of the frequency-separation, the latter are by principle limited to zones of small scales and thus effectively complement the FVM. Furthermore, the particle information allows details of the scalar quantity field to be reconstructed that extend into the sub-grid level. By using a mixing layer setup, the proposed method is tested for a range of Schmidt numbers, and the numerical costs are considered and discussed.

© 2022 Elsevier Inc. All rights reserved.

\*Corresponding author: Tel.: +49-203-3798146;  
e-mail: [michael.leer@uni-due.com](mailto:michael.leer@uni-due.com) (M. Leer)



## 1. Introduction

The simulation of scalar transport in turbulent flow is essential to describe various phenomena that are highly relevant for technical and environmental applications. Especially in connection with high Schmidt numbers, these phenomena can place great demands on the numerics, and thus require the development of more efficient methods for modelling and simulation. Emerging applications with particularly challenging Schmidt numbers include the transport of soot, nano-particles or viruses in the gas-phase. Employing a joint Eulerian-Lagrangian approach, the present study aims to reduce the increased computational effort caused by high Schmidt numbers. Due to analogies, the approach can be applied to high Prandtl numbers as well.

Every CFD simulation whose purpose goes beyond the mere solution of the flow field, typically involves the transport of one or several scalar quantities. These quantities can describe, for instance, fuel, oxidiser and (intermediate) products in a reactive flow, energy in a heat conduction problem or different liquids in a batch reactor mixing. Physically prescribed by the molecular diffusivity  $D$  and viscosity  $\nu$  of the mixing species, the Schmidt number of such systems is defined as:

$$Sc = \nu/D . \quad (1)$$

Due to its implications in the context of multi-scale behaviour, the Schmidt number becomes a decisive factor for the computational cost of a simulation if it exceeds the value of one. The Kolmogorov scale  $\eta_K$ , i.e. the smallest velocity length scale in a turbulent flow before viscosity dominates over inertia, is proportional to an expression of the Reynolds number,  $\eta_K \propto Re^{-3/4}$  [1]. In terms of a scalar quantity field, the Batchelor scale  $\eta_B$  is of equivalent interest [2],

$$\eta_B \propto \eta_K Sc^{-1/2} \propto Re^{-3/4} Sc^{-1/2} , \quad (2)$$

giving the smallest mixing length scale before molecular diffusion dominates over convection. For Schmidt numbers larger than one, the Batchelor scale is smaller than the Kolmogorov scale and scalar fluctuations will occur at scales smaller than the smallest (momentum) eddy. While both scales,  $\eta_K$  and  $\eta_B$  are comparable in gas-phase mixing ( $Sc_{\text{gas}} \approx 1$ ), Schmidt numbers are significantly higher for liquids ( $Sc_{\text{liq}} \approx 600 - 3000$ ) or two-phase flows like particle suspensions ( $Sc_{\text{particles}} \approx 10^5 - 10^6$ ) [3]. Relation (2) indicates for high Schmidt numbers that the treatment of the scalar dynamics is far more demanding in terms of spatial resolution than the treatment of momentum. This effect can be compensated by a significantly enhanced computational effort – conventionally by increasing the numerical resolution. High Schmidt number flows can be particularly challenging for Direct Numerical Simulations (DNS). The accurate scalar transport in a typical DNS liquid-mixing configuration with  $Sc_{\text{water}} = 1000$  requires according to eq. (2) a more than 30 times finer resolution, assuming an equivalent consideration as for the momentum scales. Even if the resolution is adjusted accordingly and covers all theoretical scales of mixing<sup>1</sup>, the problem of numerical diffusion remains. In order to avoid oscillatory behaviour in the scalar transport at zones of high second derivatives, typical convection discretisation schemes deliberately add diffusion into the system. This numerical diffusion scales with convective scalar fluxes. Hence, from the perspective of high Schmidt numbers, it will accumulate to relatively strong deviations from the physical scalar diffusion. The artificial smoothing caused by the transport scheme leads to massive deviations, most notably in areas of the scalar field where steep gradients or fine structures occur. Even if the initial topology is smooth and thus at first appears to allow accurate transport, strains and vortices in the momentum field and the multi-scale nature at high Schmidt numbers lead to the generation of fine structures in the scalar quantity field, which in turn lead to artificial smoothing. The previously established relationships apply analogously to heat transfer in flows. Here, the equivalent of the Schmidt number is the Prandtl number,

$$Pr = \nu/\alpha , \quad (3)$$

which relates the momentum diffusivity to the thermal diffusivity  $\alpha$ . The simulation of thermal conduction in liquid water, whose Prandtl number is typically assumed to be around 6.9 [8], will thus require considerably increased numerical resolution. An example of extremely high Prandtl numbers is glycerol ( $Pr_{25^\circ\text{C}} = 7613$ ), whose large viscosity at ambient conditions leads to a ratio of about 100 between the smallest momentum scale and the smallest temperature scale [8].

<sup>1</sup>Universal power-spectrum scaling laws of a passive scalar depending on the Schmidt and Reynolds number are still an ongoing subject of research [4, 5, 6, 7].

If unresolved, the subgrid contribution of small scales can be modelled, provided that the explicit consideration of fine structures is not decisive for the global objective of a simulation [9, 10, 11]. There is, however, a large number of applications where the neglect of small scales and artificial smoothing of the scalar field must be avoided. In chemical engineering science, for instance, there is a recurring need to mix liquid components. Such processes are typically driven almost entirely by convection. Due to the over-prediction of diffusive fluxes, traditional numerical schemes are not able to accurately predict the mixing process. Examples are the CFD simulation of stirred tanks [12] and similar reactors operating close to the supercritical condition [13]. In two-phase flows and particle suspensions, the ability to transport accurately and efficiently with respect to fine structures can be crucial to capturing the phase boundaries. An example of particle suspensions are sooting flames [14, 15, 16]. Simulating internal combustion engines, a locally precise numerical representation of the scalar quantity is essential to calculate derived properties such as pollutant formation with any confidence.

An evident approach to compensate for the disadvantages of the Eulerian FVM description concerning the convection of a scalar quantity in the range of high Schmidt numbers is to combine it with a Lagrangian description. While the Eulerian framework considers a fixed point or volume in space, where the fluid that passes through is observed, the Lagrangian Framework tracks points or particles within the flow. Since they are free of CFL stability conditions, particle methods are unaffected by numerical oscillation and are hence by principle ideally suited in the regime of high second derivatives in the field of the scalar quantity. Unlike the convective schemes used in FVM, artificial smoothing of the scalar distribution is therefore not necessary. However, in terms of describing physical diffusion, Lagrangian particles have a disadvantage compared to the Eulerian description. Their diffusion requires some form of modelling and thus represents an additional source of error. In terms of computational cost, particle methods are in general clearly disadvantaged compared to the FVM method. A joint Eulerian-Lagrangian approach should combine both frameworks in such a way that the efficiency and accuracy of the simulation is determined by the respective advantages. The mathematical coupling of the two frameworks and the computational inefficiency of particles emerge as the main challenges in implementing a hybrid method. There were numerous approaches to combine both frameworks, whereas the earliest did not yet focus on passive scalar transport. The Particle-in-Cell (PIC) method, proposed and developed by Harlow's research group [17, 18, 19, 20], is an early example where Lagrangian particles are placed in an underlying Eulerian framework. Momentum and energy properties of a fluid flow are stored and computed in the Eulerian framework, while Lagrangian particles are used to represent the fluids mass. The Marker-and-Cell (MAC) method, proposed by Harlow and Welch [21] and developed by Welch et al. [22], is distinct from the PIC method in that the transported particles act only as massless tracers and do not directly influence the dynamics of the flow. The particles can be used to visualize the flow and to track free surfaces between different phases. Approaches derived from PIC and MAC are currently widely used in computer graphics [23, 24, 25]. Lagrangian particles were applied in the context of turbulent combustion modelling – a field which is characterised by a strong coupling between transport and chemistry. The Lagrangian joint Probability Distribution Function (PDF) Method of Pope [26] decomposes fields of flow quantities, such as the chemical composition, into sets of statistically interacting particles. Through these interactions, reaction terms can be treated precisely. Lagrangian PDF methods have been widely applied with Reynolds Averaged Navier Stokes (RANS) and LES simulations [27, 28, 29, 30]. Enright et al. [31] proposed the particle level-set method, which applies Lagrangian marker particles around the interface defined by a level-set [32, 33, 34]. Rebuilding the level-set in regions which are under-resolved, the particles improve the mass conservation properties. Moreover, the particles are able to provide a local description of the interface with a higher resolution than that of the underlying Eulerian mesh. Most recently, and closer related to our proposed technique, Lagaert et al. [35] concluded from the multi-scale behaviour of turbulent scalar transport to use separate grids and different numerical methods for the scalar and the momentum. Following the work of Cottet et al. [36] in which both the momentum and scalar equations were solved by particle methods at different resolutions, they proposed a hybrid particle-spectral solver. It couples the Lagrangian scalar solution to the Eulerian momentum solution through particle re-meshing that is performed with high-order interpolation. By doing this, they detached the scalar transport from the CFL constraint and captured all mixing scales at a reasonable computational cost. Applying the hybrid particle-spectral solver, Lagaert et al. [37] studied universal scalar laws in homogeneous turbulence for a wide range of Schmidt numbers, up to  $Sc = 128$ , recovering theoretical predictions. Such a hybrid solver was applied by Santos et al. [38] in order to study differential diffusion. Making it the most related approach to our method in literature, a hybrid particle-FVM solver was also implemented and tested alongside the hybrid particle-spectral solver. In contrast to our method, however, the entire scalar quantity information is represented and transported solely by particles.

The method described in the present paper intends to provide a novel, efficient way to simulate scalar transport

up to extremely high Schmidt numbers. With the new method, the grid resolution does not need to be refined any further compared to the requirements of the momentum field. Despite this, the method provides detailed spatial subgrid information and significantly reduces numerical diffusion. The new method is based on a decomposition of the scalar quantity into an Eulerian, smooth, low-frequency component and a Lagrangian, fine-structured, high-frequency component. The former is transported alongside the momentum field by using the FVM at a grid resolution according to the Kolmogorov length-scale and the latter is described and transported by tracer particles. This Eulerian-Lagrangian decomposition principle (ELD) is founded on the assumption that regions of the scalar field which lie outside the mixing zone or that are diffusion dominated due to locally small cell-related Péclet numbers  $Pe = Re \cdot Sc$  (or  $Pe = Re \cdot Pr$  for heat transfer) can usually be transported with good accuracy by traditional FVM schemes. As high-frequency scalar information, containing sharp changes in gradient and fine structures, is often constrained to a corrugated surface in space, as found across a mixing layer or at an interface, it can be sufficient to describe only these regions using particle-based techniques. To identify such regions containing small scales, it is useful to exploit a Fourier series analogy and describe the scalar field in terms of frequencies (or wave numbers) where spatially smooth transitions correspond to low frequencies while rapidly-varying components and fine structures correspond to high frequencies. Our proposed joint Eulerian-Lagrangian method is characterised by the initial decomposition of a scalar quantity field into its high- and low-frequency components with a low-pass spatial filter. Subsequently, only the high-frequency component is translated into the Lagrangian description, whereby the information, i.e. the scalar mass, is henceforth represented by particles. Such a limited distribution of particles will significantly reduce the computational cost of the method in comparison to treating the entirety of the scalar field with Lagrangian particles. The convection of the particles is based on an interpolation of the underlying velocity field, while the diffusion is modelled by a Wiener process. The frequency-based separation between the Eulerian and the Lagrangian component is maintained throughout the simulation by continuous re-initialisation with re-filtering.

The paper is organised as follows: Details on the method and its setup are given in section 2. The Method is thoroughly tested under realistic flow conditions at different Schmidt numbers in a Mixing Layer, with the numerical setup provided in section 3 and the results presented and discussed in section 4. A conclusion in section 5 will discuss the current state of the method based on the achieved efficiency and accuracy. Also, suggestions for future work are given. In order to provide an overview of the method, Figure 1 contains a summary of the method-specific quantities as well as a broad generic flow chart.

## 2. The Euler-Lagrangian decomposition method

### 2.1. Governing equations

The motion of an incompressible, Newtonian fluid is described by the Navier-Stokes equations, which prescribe the conservation of mass and momentum within an infinitesimal flow element. In Cartesian coordinates, using index notation with the Einstein summation convention, the system of equations is:

$$\frac{\partial u_j}{\partial x_j} = 0, \quad (4)$$

$$\frac{\partial u_i}{\partial t} + u_j \frac{\partial u_i}{\partial x_j} = -\frac{1}{\rho} \frac{\partial p}{\partial x_i} + \nu \frac{\partial^2 u_i}{\partial x_j^2}, \quad (5)$$

where eq. (4) balances the mass and eq. (5) balances the three components of momentum. These equations introduce the velocity vector  $u_i$ , the fluid mass density  $\rho$  and the thermodynamic pressure  $p$  at time  $t$  and along direction  $x_i$ . The transport of a passive scalar  $\Phi$  in such a flow can be described by the following equation:

$$\frac{\partial \Phi}{\partial t} + u_j \frac{\partial \Phi}{\partial x_j} = \frac{\nu}{Sc} \frac{\partial^2 \Phi}{\partial x_j^2}, \quad (6)$$

where the first term on the left-hand-side denotes the accumulation of the scalar within the fluid element, the second term on the left-hand-side denotes the flux of scalar through the fluid elements boundary due to convection and the right-hand-side term denotes the flux due to diffusion. The diffusion is described according to the Fick law, where diffusivity is given in terms of Schmidt number and viscosity according to eq. (1). The following subsection describes the decomposition of eq. (6) into an Eulerian and a Lagrangian component.

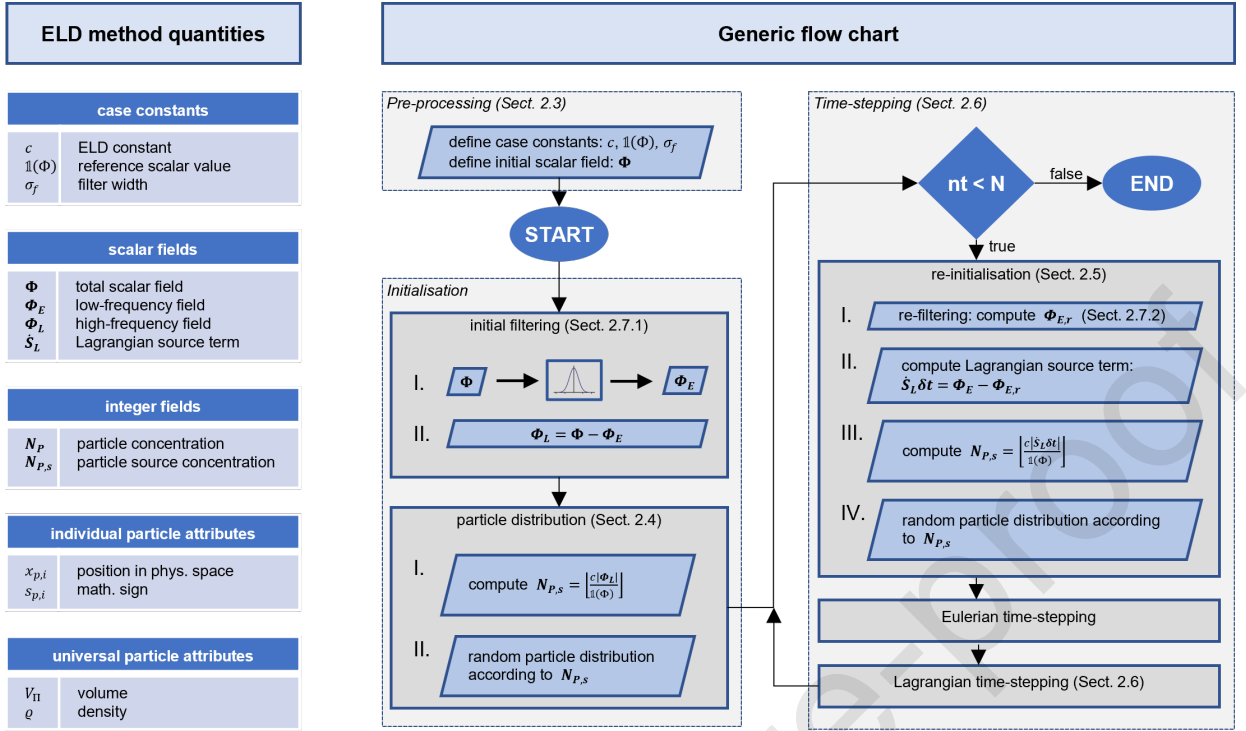


Fig. 1: The most important quantities forming the ELD method on the left alongside a generic flow chart on the right. The flow chart refers to the relevant subsections

## 2.2. Decomposition principle

The theoretical formulation of the proposed ELD method treats a conserved scalar  $\Phi$  as a summation of its low-frequency component  $\Phi_E$  and its high-frequency component  $\Phi_L$ :

$$\Phi = \Phi_E + \Phi_L, \quad (7)$$

where the high frequency component is to be transferred to the Lagrangian description later, while the low frequency component remains in the Eulerian description. Such a decomposition can be achieved with a suitable spatial low-pass filter  $h$ ,

$$\Phi_E(x_i, t) = \iiint_{-\infty}^{\infty} \Phi(x_i, t) h(x_i - x'_i) dx_i \quad (8)$$

which filters the high frequencies and thereby provides the low-frequency Eulerian field  $\Phi_E$ . Details on the chosen filters are provided in Sec. 2.7. Subsequently, the high-frequency field  $\Phi_L$  can be obtained through eq. (7) by subtracting the low-frequency component from the total component:

$$\Phi_L = \Phi - \Phi_E. \quad (9)$$

This decomposition process is schematically illustrated by Fig. 2. From eqs. (6) and (7) and due to linearity, decomposed constant density transport equations may then be written for each component of  $\Phi$ :

$$\frac{\partial \Phi_E}{\partial t} + u_j \frac{\partial \Phi_E}{\partial x_j} = \frac{\partial}{\partial x_j} \left( \frac{\nu}{Sc} \frac{\partial \Phi_E}{\partial x_j} \right) - \dot{S}_L; \quad (10)$$

$$\frac{\partial \Phi_L}{\partial t} + u_j \frac{\partial \Phi_L}{\partial x_j} = \frac{\partial}{\partial x_j} \left( \frac{\nu}{Sc} \frac{\partial \Phi_L}{\partial x_j} \right) + \dot{S}_L. \quad (11)$$

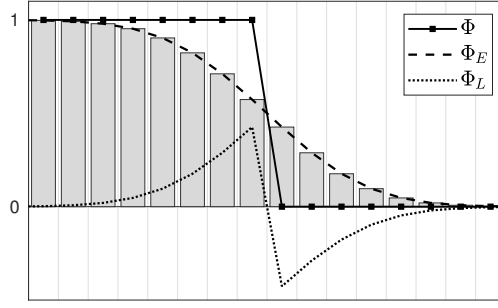


Fig. 2: Illustration of the Eulerian-Lagrangian decomposition on a 1D step function. A scalar quantity  $\Phi$  can be described as the sum of a smooth, low-frequency field  $\Phi_E$  and a rapidly-varying, high-frequency field  $\Phi_L$ . While  $\Phi$  and  $\Phi_E$  rely on a cell-centred interpolation (indicated by markers resp. grey bars),  $\Phi_L$  could be spatial-continuously approximated by particles with any required accuracy. Vertical grid lines denote boundaries of computational cells

The source term  $\dot{S}_L$  will account for any exchange of scalar information between the two phases that will be required to keep the low-frequency field suitably smooth, while maintaining overall mass conservation (sec. 2.5). Since the low-pass-filtered field  $\Phi_E$  is free of high second derivatives, it can be transported with a variety of FVM convection schemes while maintaining high accuracy and low computational cost. The high frequency component  $\Phi_L$  covers all fine structures and local details and is thus transported with Lagrangian particles. Considering high Schmidt numbers and a numerical resolution of the underlying FVM field according to the Kolmogorov length-scale  $\eta_K$ ,  $\Phi_L$  is likely to contain information at a length-scale smaller than that of the grid by orders of magnitudes. To capture and process this information, the set of particles must be able to represent the high-frequency component with any required resolution. While the low-frequency component equation (10) is solved with Eulerian methods, the high-frequency component equation (11) is never directly solved, since its contribution is covered by Lagrangian particles as described in the following.

### 2.3. Particle definition and translation

This section describes the ELD-particle definition, the Eulerian-to-Lagrangian transformation and the Lagrangian-to-Eulerian reconstruction. After the initial decomposition, the high-frequency component  $\Phi_L$  is initially present in the Eulerian description at the resolution of the FVM mesh. A primary goal is that the translation from the Eulerian description into the Lagrangian description and vice versa is subjected to mass conservation and preferably free of artificial dissipation. In the following, the definition of an ELD-particle is made according to its attributes and its translation implications from the Eulerian to the Lagrangian frame and vice versa.

Each ELD particle has four attributes. Two of them are individual and differ from particle to particle, while the other two are uniform for all particles and are defined a priori. The first individual attribute is the *position* of the particle  $p$  in physical space, given in index notation as  $x_{p,i}$ . The second individual attribute is the mathematical *sign* of the particle  $s_p$ . As shown in Figure 2, the high-frequency field  $\Phi_L$  takes on both positive and negative values. It is therefore useful to allocate a sign to the individual particles depending on whether they correct the low-frequency field  $\Phi_E$  up or down at the given point to reach the total scalar quantity  $\Phi$ . The first universal attribute is the *particle volume*  $V_\Pi$ . ELD-particles can be understood as Lagrangian fluid elements with a defined spatial extent. In the context of reconstruction – as will be described at the end of this section – the particle volume is implicitly set to that of a computational cell  $V_\Pi = \Delta^n$ , in a Cartesian mesh, in the  $n$ -dimensional simulation. The second universal attribute is the particle density  $\varrho$ . Its multiplication with the particle volume  $V_\Pi$  can be interpreted as the absolute scalar mass of a particle  $|m_p|$ , and depending on its sign  $s_p$ , this scalar mass contributes either positively or negatively to the shape of the high-frequency component at the particle position. The lower the particle density compared to the typical scalar mass per cell in  $\Phi$ , the lower the contribution of the individual particles and the greater the particle concentration required. It is explicitly defined as

$$\varrho = \frac{\mathbb{1}(\Phi)}{c}, \quad (12)$$

introducing a reference scalar value  $\mathbb{1}(\Phi)$  and the ELD constant  $c$ . The reference scalar value incorporates the dynamic range of the scalar sample space. In a zero-to-one scalar space, as used in this study, it is convenient to set  $\mathbb{1}(\Phi) = 1$ , since one is the upper bound of  $\Phi$ . Such a definition can be applied directly to real-world scalar quantities such as

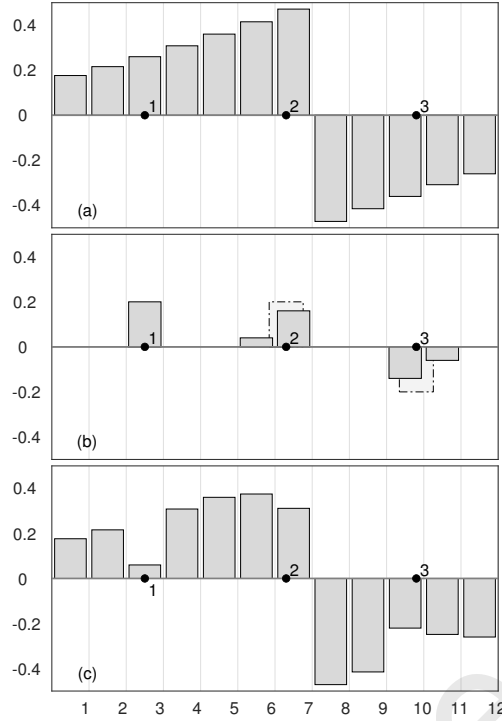


Fig. 3: Following the step function in Fig. 2, part (a) represents a section of the high-frequency field in Eulerian description. Three particles  $p = \{1, 2, 3\}$ , all with the same particle volume  $V_{\Pi} = \Delta^1 = 1$  and same particle density  $\varrho = 0.2$  (corresponding to  $c = 5$ ), with the mathematical signs  $s_p = \{+1, +1, -1\}$  are placed at the physical coordinates  $x_{p,i} = \{2.5, 6.3, 9.8\}$ . Part (b) shows Eulerian representations of the particles, where the dashed bars represent the actual particle shapes with the masses  $m_p = \{0.2, 0.2, -0.2\}$  and the solid bars represent a 2nd order reconstruction of the masses in the numerical grid. Note that particle 1 can be reconstructed exactly because its own centre is located in a cell centre, while 2nd order reconstruction leads to an artificial dissipation elsewhere. Part (c) shows the component of the field, that remained in the Eulerian description. It is obtained by subtracting the 2nd order reconstruction from the initial field. All y-axes show the scalar value and in (b) at the same time the particle density for the dashed bars

mole fractions or mass fractions. For general quantities, normalisation is practical, but not essential, defining  $\mathbb{1}(\Phi)$  as the difference between the expected upper and lower scalar space boundaries. In any case,  $\varrho$  has the same physical unit as the scalar quantity. The ELD constant  $c$  is the most significant parameter in terms of the accuracy and the computational cost of the ELD method. It is the equivalent of the amount of particles representing one unit of scalar  $\mathbb{1}(\Phi)$ , uniformly distributed over one computational cell. As will be shown in sections 2.4 and respectively 4.3, a higher ELD constant will generally deliver a more accurate Lagrangian representation and a more accurate result. However, leading to a great number of particles, it will also slow down the computation. In summary, the high-frequency component  $\Phi_L$  is transported by a set of particles representing Lagrangian elements with uniform density  $\varrho$  and volume  $V_{\Pi}$  and individual mathematical sign  $s_p$ , changing only their position  $x_{p,i}$  by passive convection and stochastic diffusion.

Figure 3 illustrates the partial transformation of a 1D scalar field from the Eulerian description to the Lagrangian description by placing three exemplary particles. It also shows the back transformation, i.e. the reconstruction of the particles into a Cartesian computational grid. As shown in this case, the reconstruction to the original FVM grid is done by means of a second-order linear interpolation, redistributing the particles mass among all cells in  $\Delta$ -vicinity, where the scalar quantity is stored at the cell centre. In the  $n$ -dimensional case, this is substituted by a second-order  $n$ -linear interpolation, i.e. a second-order trilinear interpolation in the case of a 3D simulation. As can be seen from Fig. 3 (b), such a reconstruction principle is not ideally accurate because it leads to dissipative behaviour. This loss of information can be overcome by reconstructing the particle information on a finer grid. Figure 4 describes differences in approach and accuracy between a reconstruction on the FVM grid and a reconstruction on a finer grid, where the integer refinement ratio is referred to as the reconstruction order  $f$ . The advantage of such a high-order reconstruction seems plausible considering that the particles should contain information whose spatial scale is smaller than that of the FVM grid, depending on the Schmidt number. To obtain the total field  $\Phi$  at any time during the simulation, the high-

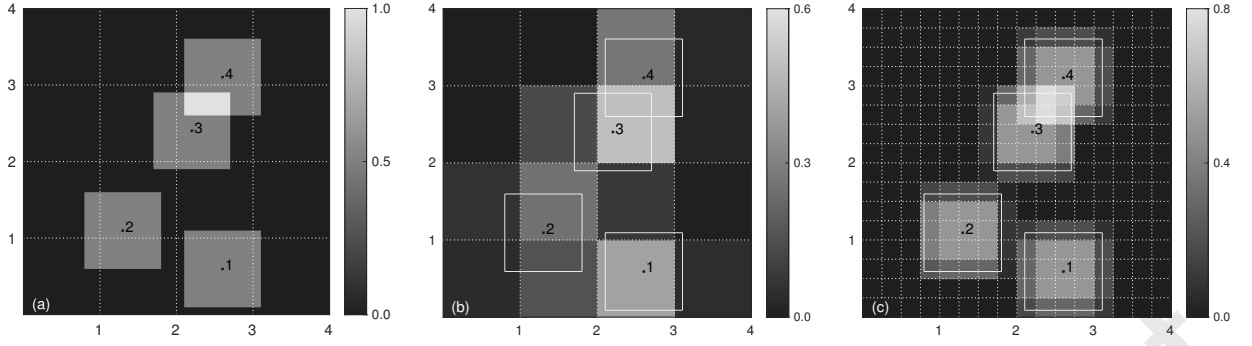


Fig. 4: Part (a) shows a 2D computational domain with four cells in each direction. Four positive ELD-particles with  $q = 0.5$  and  $V_{\Pi} = \Delta^2 = 1$  are placed at different positions. The colourmap shows the true accumulated scalar mass visualised in non-discretised, continuous representation. Part (b) shows that this continuous representation of the contribution of the particles cannot be accurately transferred to the FVM grid by applying a second order linear interpolation. The solution to this problem is a reconstruction onto a better resolved Cartesian grid, as shown in part (c). Here, the scalar mass is interpolated on a four times higher resolved grid ( $f = 4$ ), which leads to significantly higher accuracy. For  $f = \infty$  the accuracy approaches that of the mathematically ideal distribution from (a). Note that the overlap of particles (3 and 4) reveals in (c) a sub-grid structure relative to the FVM grid scale

frequency field  $\Phi_L$  must first be reconstructed as an Eulerian field and then be summed to  $\Phi_E$ . If subgrid information need to be made visible and  $\Phi_L$  has therefore been reconstructed to a finer grid,  $\Phi_E$  must be interpolated to the finer grid accordingly beforehand. Throughout the paper, a reconstruction to the original computational grid is referred to as an FVM-reconstruction, while a reconstruction to a higher resolved grid is referred to as an ELD-reconstruction. An ELD-reconstruction is suitable for representing small scales and proving their correct transport through particles. However, it is not a mandatory part of a simulation, which needs to be executed at every time step, because the subgrid information (and the high-frequency super-grid information as well) is essentially stored in the particles. Likewise, the computation of the total field  $\Phi$  is not a mandatory part of the simulation process, but may only be carried out at requested time steps or at the end of the simulation.

The ensemble of the particle properties sign  $s_p$ , density  $q$  and volume  $V_{\Pi}$  and their invariability regarding individual particles throughout the simulation leads to a strict compliance with mass conservation. The scalar mass of an ELD-particle is defined as:

$$m_p = \int_{V_{\Pi}} s_p q dV = s_p q \Delta^n . \quad (13)$$

Once a particle has been defined, its scalar mass stays the same throughout its lifetime. Since it acts as a correction of the low-frequency scalar field, the mass can take on both positive and negative mathematical signs, regardless of the sign of the total scalar quantity. Conservation applies at the level of each individual particle. As shown by Fig. 3 the initial field  $\Phi_L$  equals the sum of the particle reconstruction and a possible not converted remainder field  $\Phi'_L$ . An integration of the scalar quantity over the volumetric space of the considered particle proves conservation of mass when the remainder field approaches zero:

$$\int_{V_{\Pi}} \Phi_L dV = \int_{V_{\Pi}} \Phi'_L dV + \int_{V_{\Pi}} s_p q dV = 0 + m_p . \quad (14)$$

The conservation of mass is also confirmed numerically in section 4.1. The following section describes how the particles are distributed in the physical space so that the initial field is completely converted and also discusses the ELD-reconstruction in more detail.

#### 2.4. Particle distribution

In order to be able to represent subgrid-scales of the high-frequency field  $\Phi_L$ , the particle distribution must be able to approximate it continuously and arbitrarily accurate, depending on the chosen ELD constant  $c$ . The particle source concentration, defined as

$$N_{P,s} = \left\lfloor \frac{|\Phi_L|}{q} \right\rfloor = \left\lfloor \frac{c |\Phi_L|}{\mathbb{1}(\Phi)} \right\rfloor , \quad (15)$$

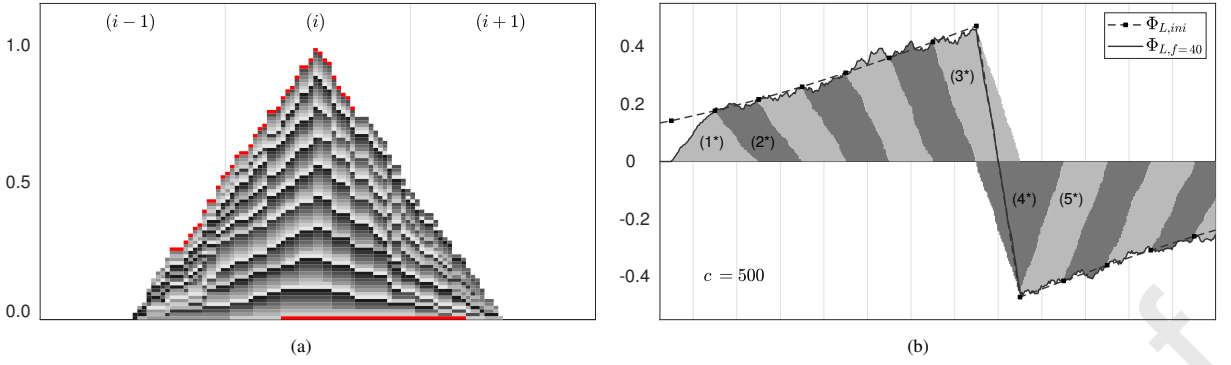


Fig. 5: Part (a) shows the effect of random particle distribution over the single one-dimensional cell ( $i$ ) with  $\Phi_L(i) = \mathbb{1}(\Phi) = 1.0$ ,  $c = 80$  and ELD-reconstruction order  $f = 40$ . According to Eq. (15) this yields the number of particles  $\phi_S(i) = 80$ , each with a scalar mass  $m_p = 0.0125$  to be randomly distributed over the cell. All particles are placed randomly regarding their own centres within ( $i$ ) and stacked up, while their scalar mass is collected in 40 numerical bins per cell. The lower red line represents the scalar mass of the first randomly placed particle. The following 78 particles are visualised in alternating shades of grey, and the upper red-coloured bins represent the last, 80th particle. This stacking leads to a triangular distribution of the total scalar mass. Part (b) shows the accumulation of such triangular distributions over several cells with  $\Phi_{L,ini}(x)$  taken from Fig. 2,  $c = 500$  and  $f = 40$ . At an arbitrarily chosen starting point ( $1^*$ ), particles are created and randomly distributed within the first cell, whereby the total number of particles necessary to match with  $\Phi_L$  at the cell centre was computed according to Eq. (15). As can be seen, the second triangle in ( $2^*$ ) overlays the one in ( $1^*$ ) in such a way that the superposition of ( $1^*$ ) and ( $2^*$ ) closely replicates the course of  $\Phi_L$  between the centres. This precise replication of  $\Phi_L$  continues throughout the following course. Particles with both, positive and negative signs are present in the immediate vicinity of the initial discontinuity in  $\Phi$  (compare with Fig. 2). Opposite particles with different signs at ( $3^*$ ) and ( $4^*$ ) cancel each other, so that the course of  $\Phi_L$  is also shown correctly here. Subsequently, the negative part of  $\Phi_L$  is reproduced by particles with negative signs ( $5^*$ )

is an integer array that gives the number of particles to be introduced per FVM cell at initialisation. The  $\lfloor \dots \rfloor$  operator denotes rounding down to the nearest integer, and taking the absolute value of  $\Phi_L$  reflects the fact that the local value of the high-frequency field may be positive or negative. Within each cell whose  $N_{p,s}$  value is not zero, the corresponding amount of particles are then distributed randomly. According to the sign of  $\Phi_L$ , the particles are assigned either a positive or a negative particle sign,  $s_p = \text{sgn}(\Phi_L(x_{p,i}))$ . Figure 5 (a) schematically illustrates the effect of random particle distribution over a single cell. For  $c \rightarrow \infty$  the distribution  $X$  over the considered cell and its neighbours becomes:

$$X = \left[ \frac{1}{8}, \frac{6}{8}, \frac{1}{8} \right]^n, \quad (16)$$

for the  $n$ -dimensional case. Considered for a single particle, this distribution suggests a strongly dissipative behaviour in the transformation from the Eulerian description to the Lagrangian description, where in the one-dimensional case 25 % in the two-dimensional case 43.8 % and in the three-dimensional case as much as 57.8 % of the scalar mass is redistributed to the surrounding cells according to Eq. (16). However, this impression becomes void as soon as the aggregation of all particles is considered, as it arises when the entire field  $\Phi_L$  is converted into Lagrangian particles. To illustrate this, the high-frequency component of the step function introduced in Fig. 2 is used. Figure 5 (b) shows, that the aggregation of all randomly placed particles for all cells, can accurately approximate the course of  $\Phi_L$ . Globally, the effect of dissipation caused by framework-translation seems to be compensated, whereby the interpolated course of  $\Phi_L$  is approximated directly and far more accurately than is possible with the FVM resolution. Depending on the choice of the ELD constant  $c$ , the reproduction of  $\Phi_L$  can achieve any desired accuracy. Figure 6 illustrates the approximation quality of  $\Phi_L$  at different ELD constants reaching from  $c = 10$  to  $c = 10000$ , using both, the FVM-reconstruction and an ELD-reconstruction with  $f = 40$  (i.e. to a grid 40 times higher resolved than the original one). Only if reconstructed to the underlying FVM grid, there seems to occur some dissipation between the cells adjacent to a discontinuity, which needs to be considered when evaluating FVM-reconstructed fields.

It is assumed that such an evenly random distribution of particles leads to the property that information can be represented and transported at much smaller length scales than the FVM grid scale would normally allow. The particle source concentration  $N_{p,s}$  is used analogously at the re-initialisation step as described in the next section to generate new particles in order to preserve the frequency-based decomposition.



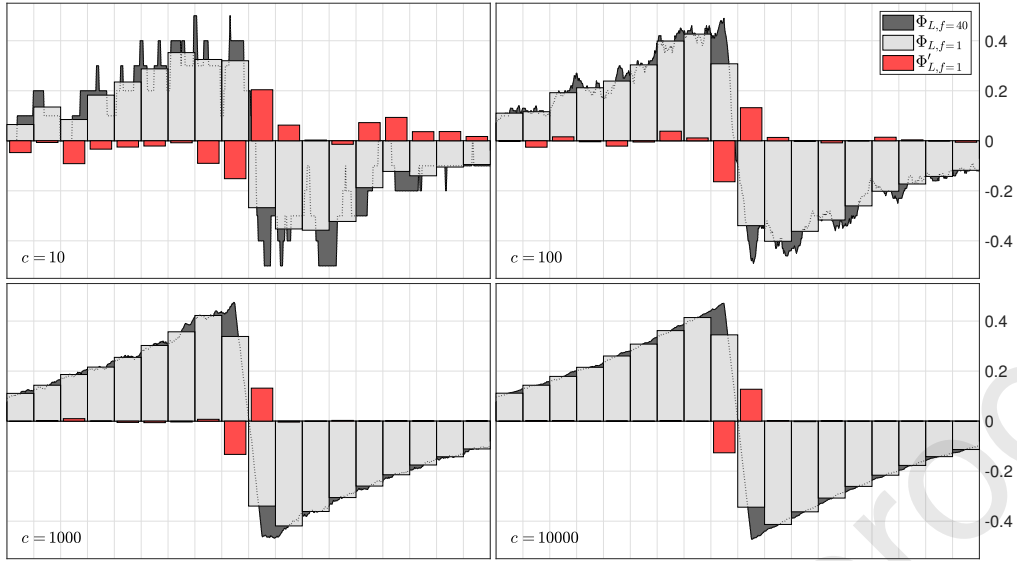


Fig. 6: Approximation of  $\Phi_L$  with different ELD constants  $c$ . ELD-reconstruction  $\Phi_{L,f=40}$ , FVM-reconstruction  $\Phi_{L,f=1}$  and FVM-reconstruction error compared to pre-decomposed course of  $\Phi_{L,ini}$  (compare with Fig. 5 (b)),  $\Phi'_{L,f=1}$ . The higher  $c$ , the more precisely the superposition of the particle reconstruction matches the course of  $\Phi_L$ . Immediately at the discontinuity in  $\Phi$  (compare with Fig. 2), there occurs dissipation between the two adjacent cells only when reconstructing to the FVM-resolution.

### 2.5. Re-initialisation concept

The method requires, that a separation between smooth and fine-structured components is maintained throughout the simulation. Directly after initialisation, these components are ideally separated, but there are mechanisms that can shift or cancel this separation over the course of the simulation. In turbulent transport at high Schmidt numbers, a viscous-convective and a viscous-diffusive subrange of mixing length scales form below the Kolmogorov length scale [39, 40, 41]. Above the Kolmogorov scale, the inertial-convective subrange forms, feeding the two aforementioned subranges down the spectrum. In the viscous-convective subrange, distortions of the fluid elements (elongation and twisting), cause local gradients of the scalar quantity concentration to become steeper. Molecular diffusion effects only become predominant in the viscous-diffusive subrange at scales below the Batchelor length scale, reducing the gradients. Starting from the inertial-convective subrange, via the viscous-convective subrange to the viscous-diffusive subrange, mixing fluctuations are continuously carried down the spectrum and the second derivative of the scalar concentration locally increases with time. This causes the second derivative to rise above the threshold in some regions of the initially smooth low-frequency field  $\Phi_E$ , leading to numerical oscillations and the damping of sub-grid scales. The low-frequency field must therefore be constantly re-filtered, whereby newly occurring high-frequency components are transferred to the high-frequency field  $\Phi_L$ . In regions of exceeding second derivatives, new particles must be created that take scalar mass away from the low-frequency field. The source term in the scalar transport equations (10 and 11) is used to handle the exchange of scalar mass. A source term in the Lagrangian phase corresponds to a sink in the Eulerian phase and vice versa:

$$\dot{S}_L \delta t = \Phi_E - \Phi_{E,r}, \quad (17)$$

with the re-filtered low-frequency field  $\Phi_{E,r}$ .

Re-initialisation takes place every time step immediately before particle transport. First the second derivative  $|\Delta^2 \Phi_E|$  of the low-frequency component is computed. A localised top-hat filter (described in section 2.7.2) that is sensitive to the second derivative is then applied on the low-frequency field to obtain the re-filtered field  $\Phi_{E,r}$ . Next, the Lagrangian source term  $\dot{S}_L$  is computed according to eq. (17). Being the equivalent to the entire high-frequency field  $\Phi_{L,ini}$  at initialisation before transformation, the time-step integrated Lagrangian source term  $\dot{S}_L \delta t$  is used to compute the particle source concentration using eq. (15). With this, the new particles are added to the existing ones and distributed analogously to the description in section 2.4. Since a smaller number of particles is generated during re-initialisation, the dissipation does not balance out as described in section 2.4. Therefore the transformation error which is apparent in the FVM-reconstruction after particle creation is added back into the Eulerian phase.

## 2.6. Time Stepping

For the convection of the low-frequency component  $\Phi_E$ , the TVD scheme with CHARM-limiter is implemented [42]. Diffusion is computed using second order central approximation of the scalar gradient at the cell faces. Temporal discretisation is carried out with the third order low-storage Runge-Kutta scheme [43]. Although the derivation of the particle motion equation including the Wiener process diffusion (eq. 21) is well known [44], it is summarised in the following because of the Wiener step adaptation to the third order Runge-Kutta scheme.

The positions of the particles are updated three times per outer time-step, in agreement with the third order Runge-Kutta scheme and using the same sub-time-step fractions  $\delta t_{sub} \in \{\delta t_1, \delta t_2, \delta t_3\}$ . At each sub-time-step, the velocity of the underlying (density-divided) momentum field  $u_i$  is interpolated in second order to the particle positions  $x_{p,i}(t)$ , based on which the particles are convected:

$$\kappa_{p,i}(t) = u_i(x_{p,i}(t), t) \cdot \delta t_{sub} \quad (18)$$

The path by which the position of a particle is shifted by convection during a sub-time-step is  $\kappa_{p,i}$ . For the diffusion of particles, a Wiener Process is applied, which represents a mathematical model for Brownian motion and aims to stochastically reproduce the diffusive motion. First, the distance probability is modelled using a normal distribution  $N$  that is a rewritten diffusion transport equation (Fick's law):

$$N(x, t) = \frac{1}{\sqrt{4\pi Dt}} \exp\left(-\frac{x^2}{4Dt}\right) \quad (19)$$

From this, the standard deviation can be determined as  $\sigma_f = \sqrt{2Dt}$ . For every particle  $p$ ,  $\sigma_f$  can be scaled with a normal distributed random number, i.e. the Wiener step  $W_{p,i}$ . The generation of such random numbers is implemented by using the Box-Muller transformation [45]. Replacing the time  $t$  by the sub-time-step  $\delta t_{sub}$  and rewriting the diffusivity as a function of the Schmidt number, one obtains the path by which the position of a particle is (randomly) shifted by diffusion:

$$\lambda_{p,i}(t) = W_{p,i} \sqrt{2 \frac{\nu}{Sc} \cdot \delta t_{sub}} \quad (20)$$

$W_{p,i}$  is updated only at the beginning of the time-step and kept unchanged throughout all three sub-time-steps. Finally, the total position update of a particle can be obtained by adding the convection path and the random diffusion path to the former position:

$$\begin{aligned} x_{p,i}(t + \delta t_{sub}) &= x_{p,i}(t) + \kappa_{p,i}(t) + \lambda_{p,i}(t) \\ &= x_{p,i}(t) + u_i(x_{p,i}(t), t) \cdot \delta t_{sub} + W_{p,i} \sqrt{2 \frac{\nu}{Sc} \cdot \delta t_{sub}} \end{aligned} \quad (21)$$

## 2.7. Low-pass filtering

The Eulerian-Lagrangian decomposition introduced in sec. 2.2 is based on the principle that the low-frequency component  $\Phi_E$  is obtained by applying a low-pass filter to the initial total field  $\Phi$  according to Eq. (8). The difference between  $\Phi$  and  $\Phi_E$  then constitutes the high-frequency component  $\Phi_L$ . The characteristics of the low-pass filter must be chosen in such a way that a spatially smooth low-frequency component, i.e. free of small length scales respectively fine structures, is produced. In order to meet the requirement for low computational effort, this component should also enable precise transport, i.e. largely without spatial oscillation or numerical dissipation, using proven, efficient FVM convection schemes at reasonable CFL numbers. To achieve these properties, a suitable quantitative threshold must be defined for filtering. For this purpose, a number of assumptions are made. The aim is to design the method in such a way that it can be superimposed on a large number of convection schemes. Schemes of high order of accuracy but low stability like the Central Differencing Schemes (CDS) of various order tend to oscillate at the presence of high second derivatives in the scalar field. High-stability schemes, such as Total Variation Diminishing (TVD) schemes, tend to become inaccurate due to numerical dissipation at sharp transitions or fine structures – basically also at high second derivatives. A low second derivative of the scalar field can thus generally be used as a marker for smoothness. If the field is filtered to the point where it can be accurately transported at a reasonable CFL count, it can be assumed that it is also sufficiently smooth so that the small scales are completely relocated to the high-frequency component. The removal of high-frequency information from a series of data results in a corresponding reduction in its second

derivative. Accordingly, a threshold for the maximum permissible absolute second derivative  $\sigma''_{max}$  can be defined, below which filtering is to be performed. With the purpose of achieving the highest possible computational efficiency, a further premise must be considered for the selection of the filter. The absolute area integral of  $\Phi_L$  is directly related to the amount of particles that have to be inserted in order to translate  $\Phi_L$  from the Eulerian description to Lagrangian particles. This connection is particularly evident in Fig. 5 (a). This means that the more scalar mass has to be "relocated" through the low-pass filter in order to smooth out discontinuities and thus extract the low-frequency component, the more particles must subsequently be introduced in the high-frequency component in order to compensate for this relocation. The consequence of this is that the filter should, if possible, smooth the scalar field at every point to the extent that the second derivative just falls below the threshold  $\sigma''_{max}$ , but does not go further down. In regions where the threshold is already met over a large area, it is logical not to filter at all. Across all situations, only a perfect filter, a Sinc filter, can fulfil this requirement. However, such a filter exists only in theory. A real filter should be defined that comes close to its properties. The structure of the method makes it useful to distinguish between two situations and to use the optimal filter in each case. Namely, the initial filtering, when a decomposition takes place for the first time before the simulation, and the filtering during re-initialisation steps, when the low-frequency component is adjusted to its target mark. The two filters used for each case are described in the following.

### 2.7.1. Gaussian filter at initialisation

In many applications of scalar transport, the topology of the initial field is characterised by an alternation of plateaus, over which the scalar quantity constantly is at its upper bound, and valleys, where it is at its lower bound, connected by step functions. In this particular case, a Gaussian filter  $h(\delta x)$  can closely correspond to a perfect filter. Defined by

$$h(\delta x) = \frac{1}{\sigma_f \sqrt{2\pi}} \exp\left(-\frac{\delta x^2}{2\sigma_f^2}\right), \quad (22)$$

it filters in the area of the discontinuities towards a target value which is related to its standard deviation  $\sigma_f$  and leaves areas further outside the discontinuities quasi unaffected. The standard deviation can be related to the previously introduced threshold  $\sigma''_{max}$ . The maximum present second derivative  $|\nabla^2 \Phi^E|_{max}$  of the Gauss-filtered field of a unit step-function is equal to the maximum gradient of the filter kernel. Differentiation of Eq. (22) yields:

$$h'(\delta x) = \frac{-\delta x}{\sigma_f^3 \sqrt{2\pi}} \exp\left(-\frac{\delta x^2}{2\sigma_f^2}\right), \quad (23)$$

$$h''(\delta x) = \left(\frac{\delta x^2}{\sigma_f^5 \sqrt{2\pi}} - \frac{1}{\sigma_f^3 \sqrt{2\pi}}\right) \exp\left(-\frac{\delta x^2}{2\sigma_f^2}\right). \quad (24)$$

Setting Eq. (24) to zero shows that the maximum gradient of the kernel will be located at  $\delta x = \sigma_f$ . Evaluating Eq. (23) at  $\delta x = \sigma_f$  yields the maximum second derivative after applying the filter as a function of the filters standard deviation.

$$|\nabla^2 \Phi^E|_{max} = \frac{1}{\sigma_f^2 \sqrt{2\pi}} \quad (25)$$

When filtering the scalar field for the first time, i.e. for the initial decomposition, the remaining maximum second derivative  $|\nabla^2 \Phi^E|_{max}$  must reach below the threshold  $\sigma''_{max}$  which was defined in advance. However, it is useful to reverse this relationship, i.e. to filter the initial field with a specified standard deviation  $\sigma_f$  in the Gauss-function and to derive the threshold  $\sigma''_{max}$  from this standard deviation with Eq. (25). This must then be adhered to during the simulation with re-initialisation procedures applying the second filter variant.<sup>2</sup> In an existing CFD workflow, it is often easier to execute the Gaussian filter not through a large kernel, but through iteratively performed diffusion steps. Guidance to such a procedure is provided by Kempf et al. [46].

<sup>2</sup>Appendix A contains a hyper-parameter study to find an optimal value for the filter width. In this, a non-universal optimum was found at  $\sigma_f = 4\Delta$

### 2.7.2. Localised diffusion filter at re-initialisation

In order to keep it below the threshold, and thus to keep the fine structures concentrated in the high-frequency component  $\Phi_L$ , the low-frequency component  $\Phi_E$  must be filtered repeatedly at the re-initialisation. The difference, i.e. the filtered out high-frequency content, is discharged to the Lagrangian phase using the source terms within the component-wise scalar transport equations eqs. (10) and (11), by re-filtering and the application of eq. (17). Since it further filters already smooth or largely dissipated regions and would thus lead to unnecessarily high particle counts, a Gauss filter is not suitable at this stage. For re-adjusting the high-frequency component  $\Phi_E$  to its target mark throughout the simulation, we propose a localised diffusion filter (Algorithm 1), which iteratively identifies and filters areas of high second derivative until the threshold is fulfilled globally. With regard to the low-frequency component  $\Phi_E$  alone, the filter does not behave globally conservative. However, this is compensated with regard to the total field  $\Phi$  through the source term  $\dot{S}_L$ . At re-initialisation,  $\dot{S}_L$  acts analogous to  $\Phi_L$  at initialisation and the same particle creation procedure as introduced in sec. 2.3 and sec. 2.4 can be used, adding the new particles to the existing ones.

---

**Algorithm 1:** Localised diffusion filter
 

---

**Data:**  $\Phi_E, \sigma''_{max}, DS$  (diffusion stability criterion)

**Result:**  $\Phi_E$  (re-filtered),  $\dot{S}_L \delta_t$

- 1 Keep original (not re-filtered) field:  $\Phi_{E,old} = \Phi_E$  ;
  - 2 Compute 2<sup>nd</sup> derivative:  $\nabla^2 \Phi_E = \partial^2 \Phi_E / \partial x_j^2$  ;
  - 3 Compute maximum 2<sup>nd</sup> derivative:  $|\nabla^2 \Phi_E|_{max}$  ;
  - 4 **while**  $|\nabla^2 \Phi_E|_{max} > \sigma''_{max}$  **do**
  - 5     Compute diffused field:  $\Phi_{E,diff} = \Delta^2 \cdot DS \cdot \nabla^2 \Phi_E$  ;
  - 6     Merge diffused field with former field. Take scalar value of diffused field, where  $|\nabla^2 \Phi_E|_{max} > \sigma''_{max}$  and keep former scalar value elsewhere:  $\Phi_E = \text{merge}(\Phi_{E,diff}, \Phi_E, |\nabla^2 \Phi_E| > \sigma''_{max})$  ;
  - 7     Update:  $\nabla^2 \Phi_E$  ;
  - 8     Update:  $|\nabla^2 \Phi_E|_{max}$  ;
  - 9 **end**
  - 10  $\dot{S}_L \delta_t = \Phi_{E,old} - \Phi_E$  ;
- 

## 3. Numerical setup and test case configuration

In this study, a three-dimensional computational domain is used to provide a realistic turbulent energy cascade. Because of the particle motion equation depending on a well-chosen velocity field resolution, careful consideration of turbulence scales is necessary. Section 3.1 provides general information about the computational domain and the numerical settings for all simulations. While the momentum field is kept the same, different parameters regarding the ELD method are varied and tested. Section 3.1 describes the different test cases.

### 3.1. Flow field setup and simulation numerics

The computational domain spans  $D_x = D_y = D_z = 6 \text{ mm} = 120 \eta_K$  in x-, y-, z-direction, respectively. It is discretised by a Cartesian grid with a constant length interval of  $\Delta = 25 \mu\text{m} = 0.5 \eta_K$  resulting in a total of 13.8 M cells. Periodic boundary conditions are applied in all directions. Viscosity and density are set constant with the properties of air at 298.15 K and 101.325 kPa. The initial flow field consists of two horizontal streams of equal but opposite momentum, separated at  $y = \frac{1}{4} D_y$  and  $y = \frac{3}{4} D_y$ , respectively. The inner stream, corresponding to  $\frac{1}{4} D_y \leq y < \frac{3}{4} D_y$ , is initialised with a mean velocity of  $+U_0 = 3.0 \text{ m s}^{-1}$  and a uniform scalar value of  $\Phi = 1$ . The outer flow, bridging the periodic boundary at north and south direction, is initialised with a velocity of  $-U_0 = -3.0 \text{ m s}^{-1}$  and a uniform scalar value of  $\Phi = 0$ . The velocities and the physical extent of the domain were chosen such that an adequate resolution of the turbulent scales can be expected. Under the given settings, the Kolmogorov length is about  $\eta_K = 50 \mu\text{m}$  and is thus twice the grid spacing. Appendix B provides further details and justification on the chosen settings. In order to stimulate the rapid growth of shear layer instabilities, the initial velocity profile is superimposed by isotropic velocity

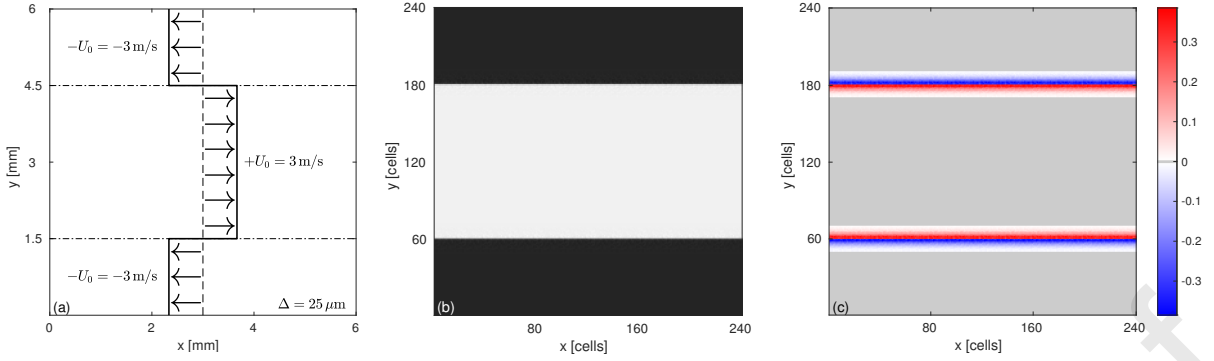


Fig. 7: Part (a) shows the initial mixing layer mean flow profile normal to the z-direction. Periodic boundaries are applied in all directions. Part (b) shows the reconstructed total scalar field  $\Phi$  after initialisation, where white colour denotes  $\Phi = 1$  and black colour denotes  $\Phi = 0$ . Note the reconstruction noise at the boundary layers. Part (c) shows the initial high-frequency field on a z-normal cross-section. Computational cells with  $\Phi_L = 0$  and thus with zero particles are coloured grey

perturbations of  $\overline{u'u'} = \overline{v'v'} = \overline{w'w'} = 0.09 \text{ m}^2 \text{ s}^{-2}$  with a length scale of  $0.25 \text{ mm}$ , generated using the methods by Klein et al. [47] and Kempf et al. [48]. Figure 7 illustrates the domain and the initial mean velocity distribution as well as the high-frequency component field right after the initialisation. Such a mixing layer setup simulates free shear layer situations in real-world turbulent flows. Related configurations are therefore frequently applied for the testing of new methods [49, 50]. The velocity shear leads to Kelvin Helmholtz instabilities which in turn lead to highly complex, chaotic structures. These will cause great distortions of the scalar field, making it possible to thoroughly test the proposed ELD method.

The ELD-method is implemented into the massively parallel finite volume LES/DNS code PsiPhi [51, 52] in its low-Mach version. Momentum fields are discretised with a second-order central differencing scheme (CDS) for the convective term and second-order accurate approximation for the diffusive term. A third-order accurate low-storage Runge–Kutta scheme proposed by Williamson [43] is applied for time integration. Particle convection and diffusion are split up in sub time steps, according to the Runge-Kutta scheme. The pressure Poisson-equation is solved by a preconditioned conjugate gradient (PCG) solver. A CFL number of 0.5 is employed. The simulation is run on 2160 Xeon E5-2650 cores on the magnitUDE supercomputer. Details about the resulting momentum field including velocity profiles at different time steps are provided in appendix B.

### 3.2. Test cases

Setting different ELD-constants, the scalar field solution of the ELD-method is compared with the solutions of the TVD schemes applying the SUPERBEE [53] delimiter for a range of different Schmidt numbers. The momentum field and its temporal evolution always remain the same according to the description in section 3.1. This results in different scalar field solutions for the same momentum field, allowing a precise and meaningful comparison of the applied methods. In order to enable a correct comparison of the simulation time and thus the computational costs, the momentum field and thus the entire CFD workflow is repeatedly simulated alongside that of the scalar transport, even if it does not change. For the Schmidt numbers 16, 100, 1000 and infinity, one SUPERBEE simulation and 5 ELD simulations are performed each. The ELD constants  $c$  set for the ELD simulations are 32, 64, 128, 256 and 512 respectively, which means that 32 to 512 particles are used to represent the full scalar content of a single cell as described in section 2.4. This results in a total of 24 simulations, i.e. 24 different results of the scalar field for an identical momentum field. Table 1 summarises the test cases.

## 4. Results

The simulation cases listed in the previous section are analysed and compared with each other. Comparisons are made with regard to the method (SUPERBEE vs. ELD) and the parameters set (Schmidt number and ELD-constant  $c$ ). The FVM reconstruction, the ELD reconstruction, the influence of the ELD constant  $c$  in connection with the Schmidt number and the costs of the method are discussed in the following. Since decaying turbulence is present, and the mixing progress increases in time, visualisations of the scalar field are shown for several time steps, typically

|                 |               |               |               |               |
|-----------------|---------------|---------------|---------------|---------------|
| Sc              | 16            | 100           | 1000          | inf           |
| $\eta_B/\Delta$ | 0.5           | 0.2           | 0.063         | 0.0           |
| Method:         |               |               |               |               |
| SUPERBEE        | <i>SB-1</i>   | <i>SB-2</i>   | <i>SB-3</i>   | <i>SB-4</i>   |
| ELD ( $c=32$ )  | <i>ELD-1</i>  | <i>ELD-2</i>  | <i>ELD-3</i>  | <i>ELD-4</i>  |
| ELD ( $c=64$ )  | <i>ELD-5</i>  | <i>ELD-6</i>  | <i>ELD-7</i>  | <i>ELD-8</i>  |
| ELD ( $c=128$ ) | <i>ELD-9</i>  | <i>ELD-10</i> | <i>ELD-11</i> | <i>ELD-12</i> |
| ELD ( $c=256$ ) | <i>ELD-13</i> | <i>ELD-14</i> | <i>ELD-15</i> | <i>ELD-16</i> |
| ELD ( $c=512$ ) | <i>ELD-17</i> | <i>ELD-18</i> | <i>ELD-19</i> | <i>ELD-20</i> |

Table 1: A total of 24 test cases are simulated. Included for each value of Sc are the corresponding Batchelor scales, with respect to  $\Delta$ , considering a Kolmogorov length-scale of  $\eta_K = 50 \mu\text{m}$ .

1500, 2000 and 3000. At these time steps the turbulent Reynolds numbers are 333, 194 and 49 respectively, where the first number is also at the peak of turbulence. Appendix B goes into more detail about the temporal course of the turbulence.

#### 4.1. FVM-resolved reconstruction

For a Schmidt number of 1000, Fig. 8 visualises the scalar field as a solution of the classical FVM simulation, the solution of the ELD method as well as the low-frequency and high-frequency components for the time steps 0, 1500, 2000, and 3000. In general, the visualisations of the ELD solution appear richer in contrast to those of the SUPERBEE reference, considering the grey-scale colourmap. In addition, the transitions between plateaus, i.e. regions with a high scalar value, and regions with a low scalar value are more pronounced, which indicates a significantly reduced numerical diffusion. On closer observation, additional smaller mixing scales become apparent in the ELD case that are missing in the SUPERBEE reference. These differences continue across all time steps. Based on the grey-scale, it can be seen in time step 3000 that the ELD solution not only contains significantly smaller scales and is far more detailed, but also that the total range of the scalar values is larger and thus completely unmixed regions still exist. The field of the low frequency component  $\Phi_E$  is consistently smooth. This property is required for the accurate TVD-based simulation of  $\Phi_E$ . The high-frequency components that were filtered out of the low-frequency field can be found in the high-frequency component  $\Phi_L$ . This takes on both positive and negative values, depending on whether the low-frequency field has to be corrected up or down at the corresponding point in order to obtain the correct total field  $\Phi$ .

In Fig. 9 one-dimensional samples of the scalar fields are plotted. The line along which the plot is made corresponds to the mid-vertical line on the cross-sections previously shown in Fig. 8. These plots confirm the impression from the previous scalar field visualisations, that the solution of the ELD method contains smaller scales and overall finer structures than the SUPERBEE reference. The reference solution also appears much smoother in this representation. Considering the whole field, the PDFs (Fig. 8) confirm that in the SUPERBEE case the mixing process is more advanced at any regarded time-step, as a larger proportion of the points have a scalar value in the range of 0.5. However, especially at the beginning of the simulation there are points where the scalar field of the ELD solution falls below or exceeds the physically prescribed range of 0 to 1. This is due to the fact that with a finite ELD-constant, noise occurs during reconstruction, as already illustrated by Fig. 6. The ELD method is not bounded.

As already mentioned in section 2.3, it can be confirmed numerically that the ELD method is mass conservative. This property can be verified by averaging the scalar value over the entire 3-dimensional field. Since half of the field was set to 1 and the other half to 0 during initialisation, and neither sources nor sinks exist in the periodic domain, the mean scalar value must always be 0.5, regardless of the mixing progress. A deviation from this value can be expressed as:  $(\bar{\Phi} - 0.5)/0.5$ . The maximum deviation found over all 20 ELD simulations and all time steps is 0.0014961%. This is the confirmation that mass conservation is globally respected throughout decomposition, re-initialisation and reconstruction.

#### 4.2. ELD-reconstruction

Figure 10 illustrates a comparison of the SUPERBEE reference and the ELD-reconstruction with order 1 (i.e. a resolution at the original FVM level) with an ELD-reconstruction of order 8, i.e. a reconstruction towards an 8-

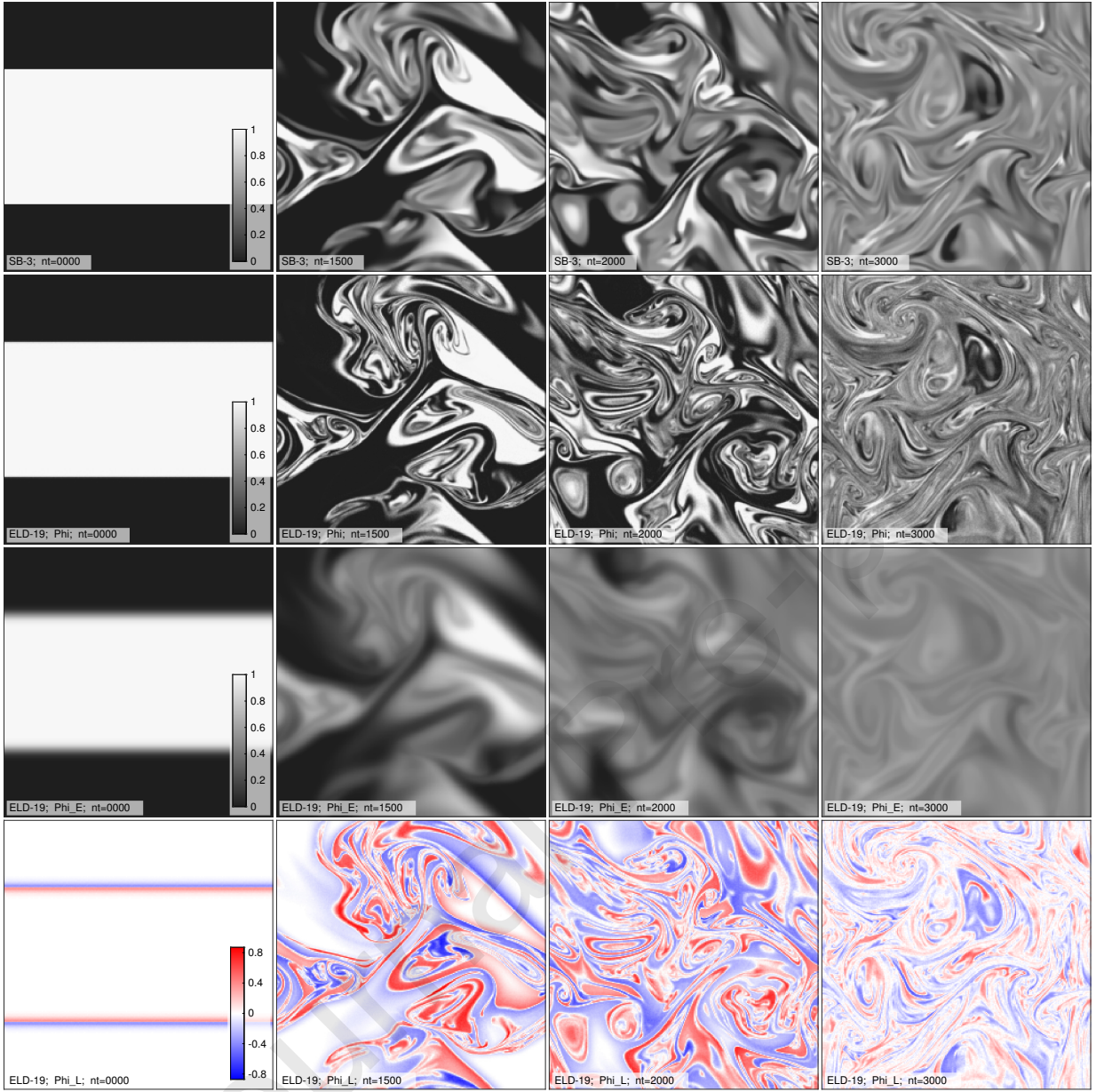


Fig. 8: A comparison of the classical FVM approach with the ELD-method for  $Sc = 1000$ . From top to bottom: Case SB-3 (SUPERBEE reference), Case ELD-19 ( $c = 512$ ), the low-frequency component  $\Phi_E$  of ELD-19 and the high-frequency component  $\Phi_L$  of ELD-19. From left to right, the time steps 0, 1500, 2000 and 3000. The grey-scale colourmap axis for the first two rows reaches from 0 to 1 (the colour white corresponds to a scalar value of 1). Z-wise cross-sections are shown

fold resolution compared to the original resolution, for a section of the scalar field ( $Sc = 1000$ ) previously shown in Fig. 8 for the time step 2000. In this zoomed-in view, the result of the ELD reconstruction becomes clear and a physically meaningful representation of the small scales is proven. At  $f = 8$  in the 2-dimensional view, one cell of the FVM-reconstruction equals 64 pixels in the ELD-reconstruction. Latter is significantly more contoured regarding the grey-scale colourmap. Fluid packages of high and low scalar values that encounter each other only at this moment or recently are well separated from each other. Typical structures of small scales at high Schmidt numbers are recognisable, such as elongated filaments which are known from experiments [54, 55].

Smaller mixing scales are expected at higher Schmidt numbers. Accordingly, there must be a relationship between the Schmidt number and the ELD reconstruction order  $f$ . The higher the Schmidt number, the greater the reconstruc-



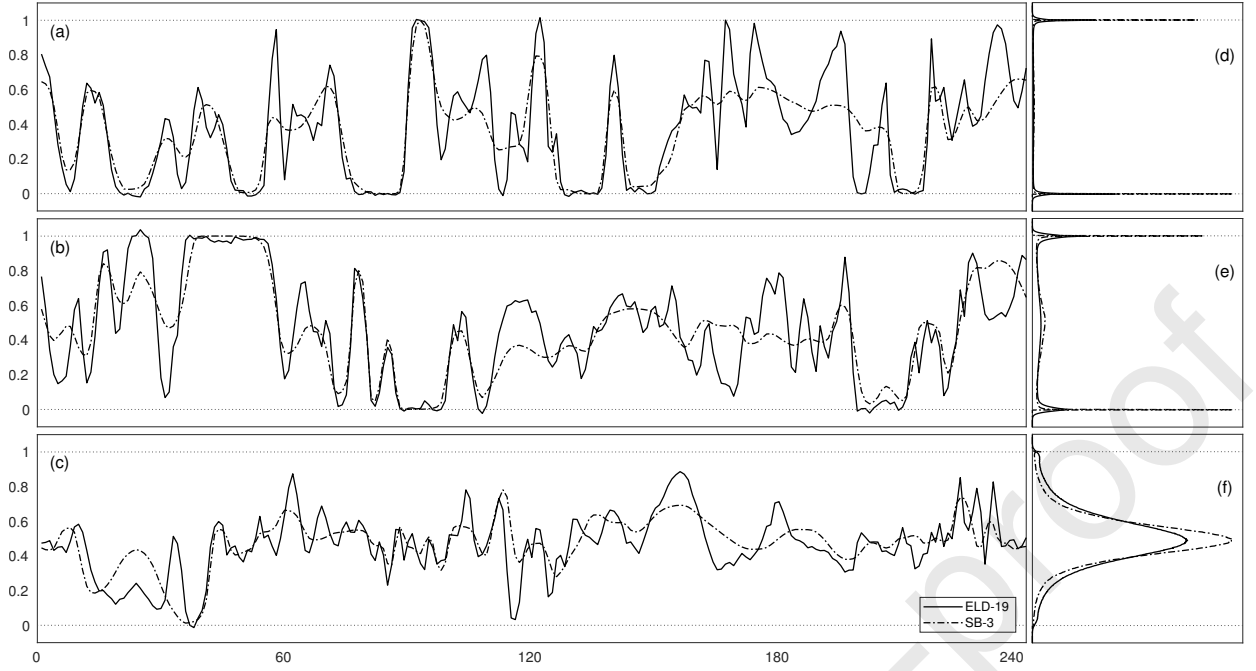


Fig. 9: Plots of the scalar quantity along a one-dimensional line that vertically spans the cross-sections shown in Fig. 8 at the centre for the time-steps 1500, 2000 and 3000 in (a), (b) and (c) respectively. Probability density functions for the scalar value are shown, considering the entire field, for the same time-steps in (d), (e) and (f) respectively. Solid line: Eulerian-Lagrangian decomposition, dotted line: Eulerian SUPERBEE.

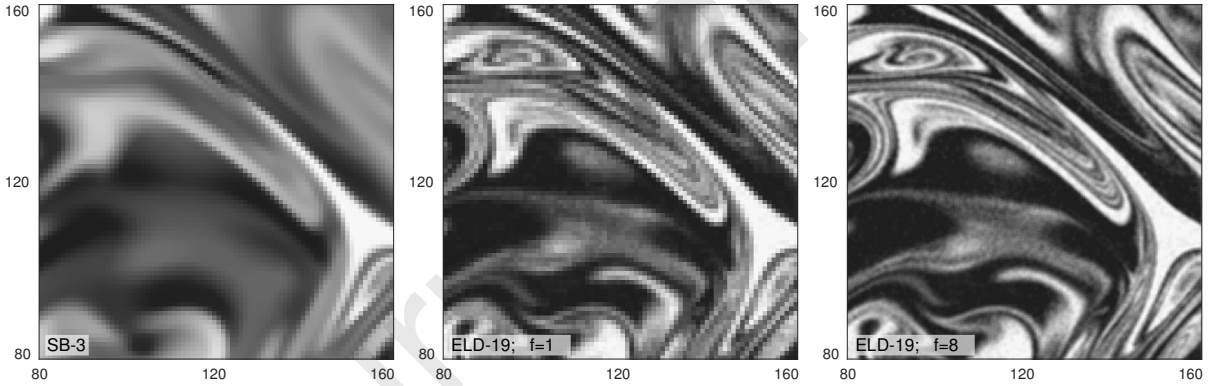


Fig. 10: A 2-dimensional 80x80 FVM-cells slice of the scalar field at time step 2000 and  $Sc = 1000$  is shown as the solution of the SUPERBEE reference, as the solution of the ELD simulation ( $c = 512$ ) with FVM-reconstruction (i.e.  $f = 1$ ) and as the same with ELD-reconstruction ( $f = 8$ ). Grey-scaled colour-map reaches from 0 (dark) to 1 (light)

tion order must be chosen to cover all the mixing scales that are actually transported. Expressed differently, higher Schmidt numbers bring the potential for finer reconstructions. By selecting an even smaller 2-dimensional section of the scalar field at  $nt = 2000$  ( $35 \times 25$  FVM cells) this relationship is studied visually. Figure 11 shows the results of the ELD reconstruction for all Schmidt numbers examined, testing different reconstruction orders in each case. At  $Sc = 16$ , the ELD reconstructions generally appear to be noisy. At  $Sc = 100$  the ELD reconstruction is less noisy, a slight increase in detail from  $f = 2$  to  $f = 4$  can be observed. After that, the reconstruction seems to be saturated: No further details are visible at  $f = 10$ . The situation is different with  $Sc = 1000$ , here an improvement in the level of detail is visible in the transition from  $f = 4$  to  $f = 10$ . This improvement is more significant for  $Sc = \infty$ . It is therefore apparent that a finer reconstruction can be meaningful in the case of higher Schmidt numbers. With smaller Schmidt numbers, there is the problem of noise, which is discussed in more detail in section 4.3.

To quantify the relationship between Schmidt number and potentially meaningful reconstruction order, a measure is defined that expresses the gain of an ELD simulation over its reference SUPERBEE simulation. This is based on



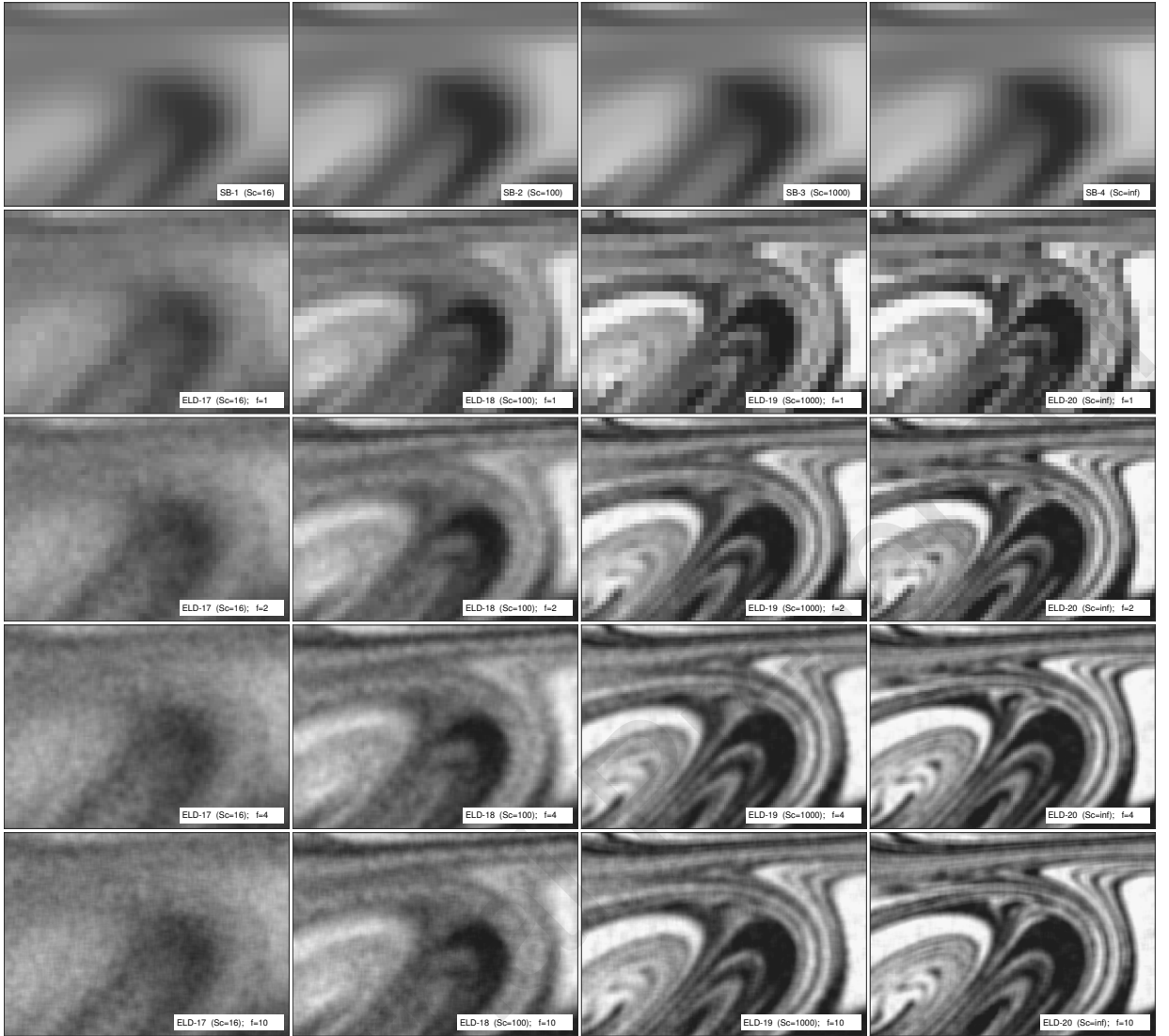


Fig. 11: A 2-dimensional slice of the size  $35 \times 25$  FVM cells, of the scalar field at time-step 2000 reconstructed by using different reconstruction order. From left to right: Schmidt numbers are 16, 100, 1000 and infinity. From top to bottom: SUPERBEE references, FVM-reconstruction of ELD-solution ( $f = 1$ ) and ELD-reconstructions of the same with  $f = 2$ ,  $f = 4$  and  $f = 10$ . ELD cases with  $c = 512$  are used. Grey-scaled colour-map reaches from 0 (dark) to 1 (light)

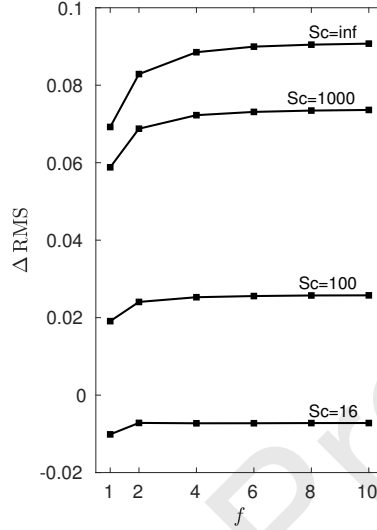
the root mean square (RMS) of the scalar field, as this quantifies the *unmixedness* and can thus compare the total diffusivity of different methods. In general, it can be argued that for the same physical boundary conditions, the method with the higher RMS at a given time step is the one with the lower total diffusivity. According to the images in Fig. 11, table 2 lists the RMS for each combination of method, Schmidt number and, if applies, reconstruction order. From these, to compare the RMS of the ELD solution directly with the RMS of the SUPERBEE reference, the following measure is defined:

$$\Delta\text{RMS} = \left( \overline{((0.5 - \Phi)^2)}^{0.5} \right)_{\text{ELD}, \text{Sc}, c} - \left( \overline{((0.5 - \Phi)^2)}^{0.5} \right)_{\text{SB}, \text{Sc}}. \quad (26)$$

The resulting values of  $\Delta\text{RMS}$  are plotted over the reconstruction order for different Schmidt numbers in Fig. 12. The ELD simulations with  $\text{Sc} = 16$  perform worse than the reference simulation which, however, could be related to the over-compressive behaviour of SUPERBEE and its effect on the chosen metric. For the other Schmidt numbers an advantage can be seen. When comparing the curves for the Schmidt numbers 100, 1000 and infinity, it becomes

| $f \backslash Sc$ | 1     | 2     | 4     | 6     | 8     | 10    | SB    |
|-------------------|-------|-------|-------|-------|-------|-------|-------|
| 16                | 0.152 | 0.155 | 0.155 | 0.155 | 0.155 | 0.155 | 0.162 |
| 100               | 0.215 | 0.219 | 0.221 | 0.221 | 0.221 | 0.211 | 0.195 |
| 1000              | 0.262 | 0.272 | 0.275 | 0.276 | 0.276 | 0.277 | 0.203 |
| inf               | 0.273 | 0.286 | 0.292 | 0.293 | 0.294 | 0.294 | 0.204 |

Table 2: Comparison of RMS for different Schmidt numbers and reconstruction orders, covering the same combinations as shown in Fig. 11

Fig. 12: Gain of ELD-simulations over the respective reference SUPERBEE simulations expressed as  $\Delta RMS$  over a range of reconstruction orders  $f$ 

apparent that the saturation point shifts towards increasing reconstruction orders. Hence, this confirms the visual analysis in Fig. 11. However, due to the noise generated by the reconstruction of the Lagrangian particles into the Eulerian framework, this form of quantification may not be satisfactory. The noise becomes more pronounced the closer it is zoomed into the field (compare with Fig. 6). Regardless of the quantification chosen, especially when assessing the finest structures with high reconstruction orders, noise will affect the analysed quantity. Figure 13 shows that even on an extremely small slice and with a very high reconstruction order, small, meaningful structures are still recognisable, even if they are heavily overlaid by small-scaled noise. Note that there is still a form of numerical diffusion, which becomes apparent at this level of zoom. Theoretically, there should not exist any intermediate values of the scalar quantity for an infinite Schmidt number.

#### 4.3. Schmidt number and ELD constant

Having investigated the relationship between the Schmidt number and the ELD-reconstruction order in the previous section, this section looks at the relationship between the Schmidt number and the ELD-constant  $c$ . Figure 14 illustrates a comparison of the SUPERBEE reference and different settings of  $c$ , for a section of the scalar field ( $Sc = 1000$ ,  $nt = 2000$ ). A comparison of the three different ELD constants shows a trend towards better level of detail but also towards less reconstruction noise for larger values. The noise appears in the form of dot-shaped errors that extend over approximately one cell length. This is consistent with the findings on the approximation error of the high-frequency field under low ELD-constants as illustrated in Fig. 6. Since the computational cost grows slightly over-proportionally with the ELD-constant (see section 4.4), it is relevant to understand whether even small constants can deliver results that provide enhanced value compared to classical FVM simulations, despite the noise that they are causing. This could be the case if a method is required that has a greatly reduced numerical diffusivity at computational costs comparable to an FVM simulation, whereby the small scales are substantially transported in the background but do not have to be resolved in an ELD reconstruction. It is assumed that in an FVM reconstruction

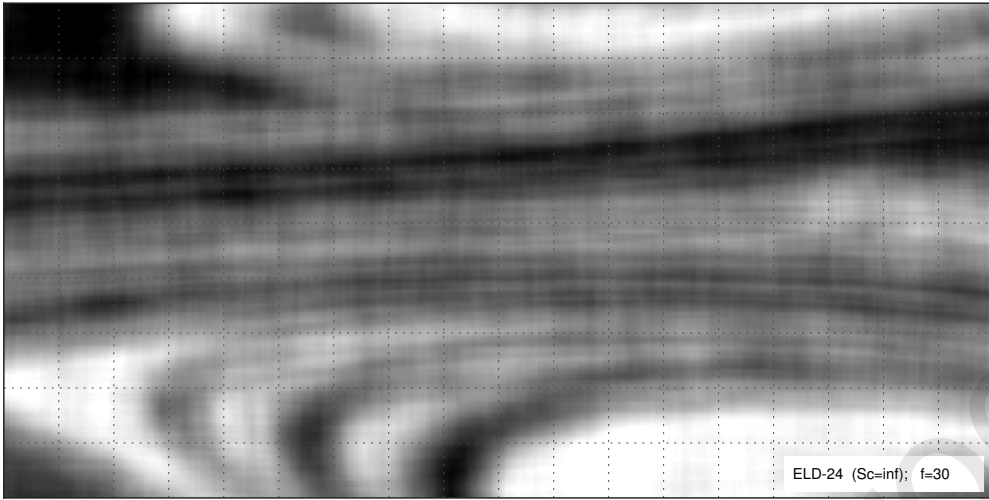


Fig. 13: A very small 2D-slice ( $18 \times 9$  cells) at time-step 2000 simulated for an infinite Schmidt number and with the ELD-constant  $c = 512$ . ELD-reconstructed with order  $f = 30$ . Dotted lines indicate the edges of the original FVM mesh. Grey-scaled colour-map reaches from 0 (dark) to 1 (light)

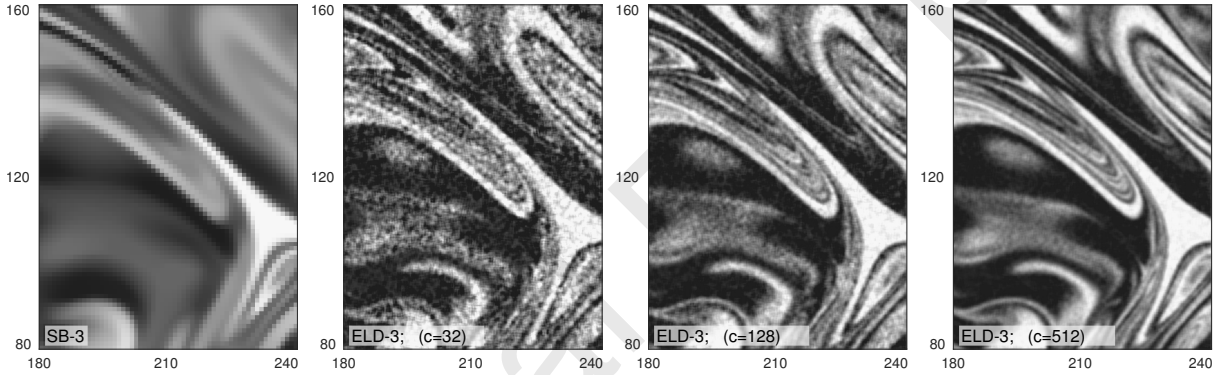


Fig. 14: A similar 2-dimensional slice (60x80 FVM-cells) of the scalar field as used for Fig. 10 ( $Sc = 1000$ ) is shown here as the solution of the SUPERBEE reference and as the solution of three ELD-simulations with ELD-constants  $c = 32$ ,  $c = 128$  and  $c = 512$ , respectively. ELD-reconstruction order is set as  $f = 8$ . Grey-scaled colour-map reaches from 0 (dark) to 1 (light)

of the ELD simulation, the noise described above is at least partially filtered by the 2nd order trilinear interpolation of the particle scalar mass on the FVM grid. Figure 15 shows different combinations of Schmidt numbers and ELD-constants, whereby for the ELD cases an ELD-reconstruction of the order  $f = 8$  is used. Due to still existing noise, the ELD method seems to not offer significant higher value compared to the SUPERBEE reference for  $Sc = 16$ . However, from  $Sc = 100$ , a low ELD-constant of  $c = 32$  provides much better detail on the grid scale than the reference. A comparison with  $c = 128$  and  $c = 512$  also shows that the level of detail is comparable with those and that the scalar quantity is similarly well resolved apart from the noise. Provided that noise is not an obstacle, even a low-cost simulation with  $c=32$  could be a relevant alternative to FVM simulations with SUPERBEE. Apart from that, there are also possibilities conceivable to filter out the noise and still maintain a better resolution.

When fine reconstruction is important, and the smallest mixing scales not only have to be transported correctly, but also resolved, a high particle concentration seems unavoidable. To illustrate this, Fig. 16 again refers to a small 2D section of the scalar field, where this is highly resolved for different combinations for Schmidt numbers and ELD-constants with an ELD-reconstruction. As expected, the noise decreases towards larger ELD-constants.

Due to the noise, it is difficult to establish a quantitative relationship between the Schmidt number and the required ELD-constant. This also depends on the demands placed on the high-resolution field. Figure 17 shows the time series of the averaged scalar dissipation rate for all simulated cases with finite Schmidt number.

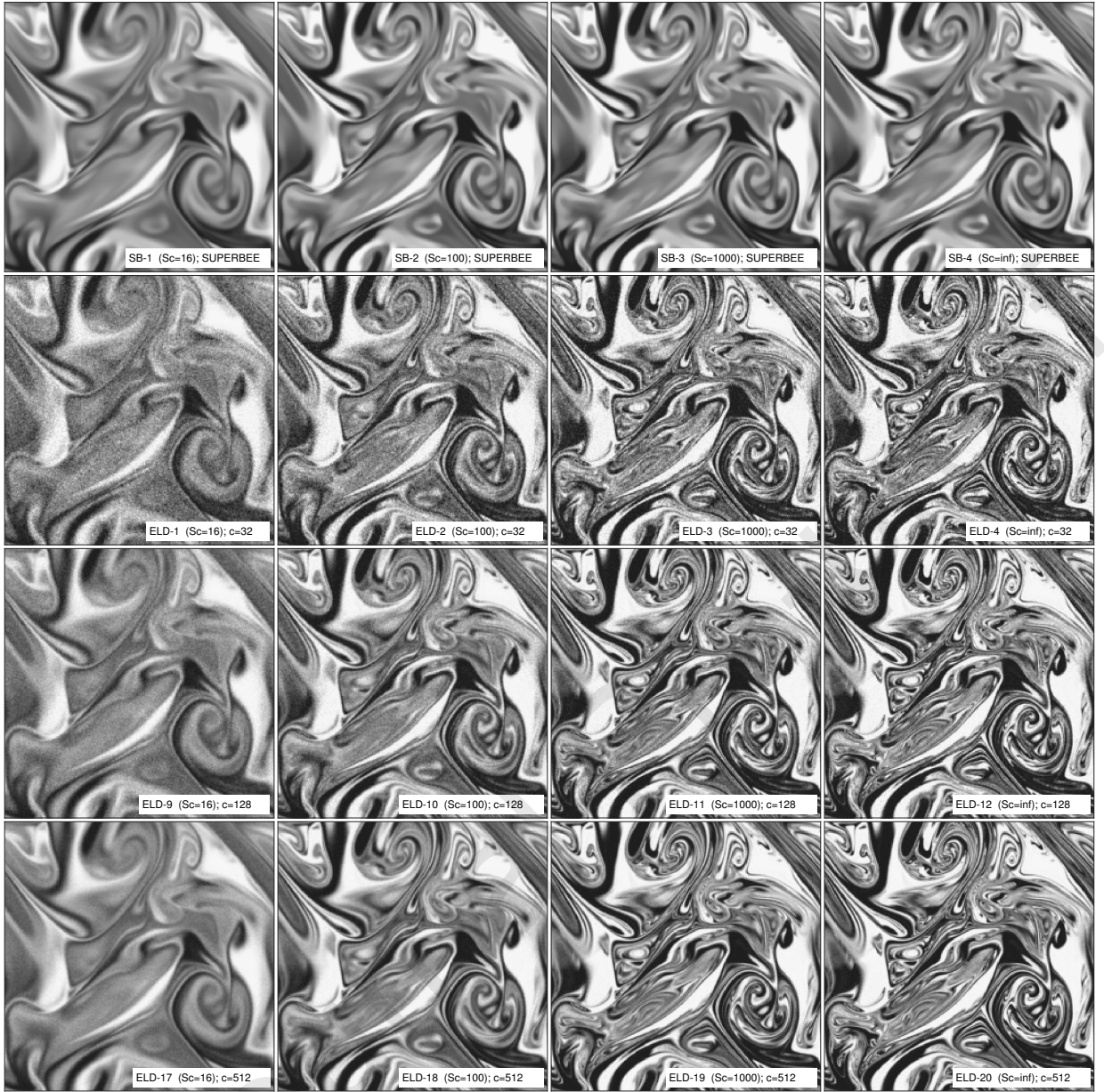


Fig. 15: Full  $z$ -wise cross-sections of the scalar field at time-step 2000 for different combinations of  $Sc$  and  $c$ . From top to bottom: SUPERBEE reference solutions and ELD-solutions from simulations with the constants  $c = 32$ ,  $c = 128$  and  $c = 512$ , respectively. From left to right: Schmidt numbers  $Sc = 16$ ,  $Sc = 100$ ,  $Sc = 1000$  and  $Sc = \infty$ . ELD-reconstruction order in all ELD-solutions is set to  $f = 8$ . Grey-scaled colour-map reaches from 0 (dark) to 1 (light). Note, that the Kolmogorov length scale is over-resolved by more than a factor of two at this time-step, which leads to an untypically good SUPERBEE performance

#### 4.4. Computational cost

Table 3 gives the computation time, the computational cost expressed in form of CPU hours and, if applies, the maximum particle count for each test case. As expected, the ELD simulations exceed the SUPERBEE simulations considerably in terms of computational costs. A correlation between the ELD constant, the maximum number of particles and the costs is apparent. A high ELD-constant implies a proportionally high particle concentration, which in turn implies a high computational cost. The Schmidt number has no significant effect on the duration of either the

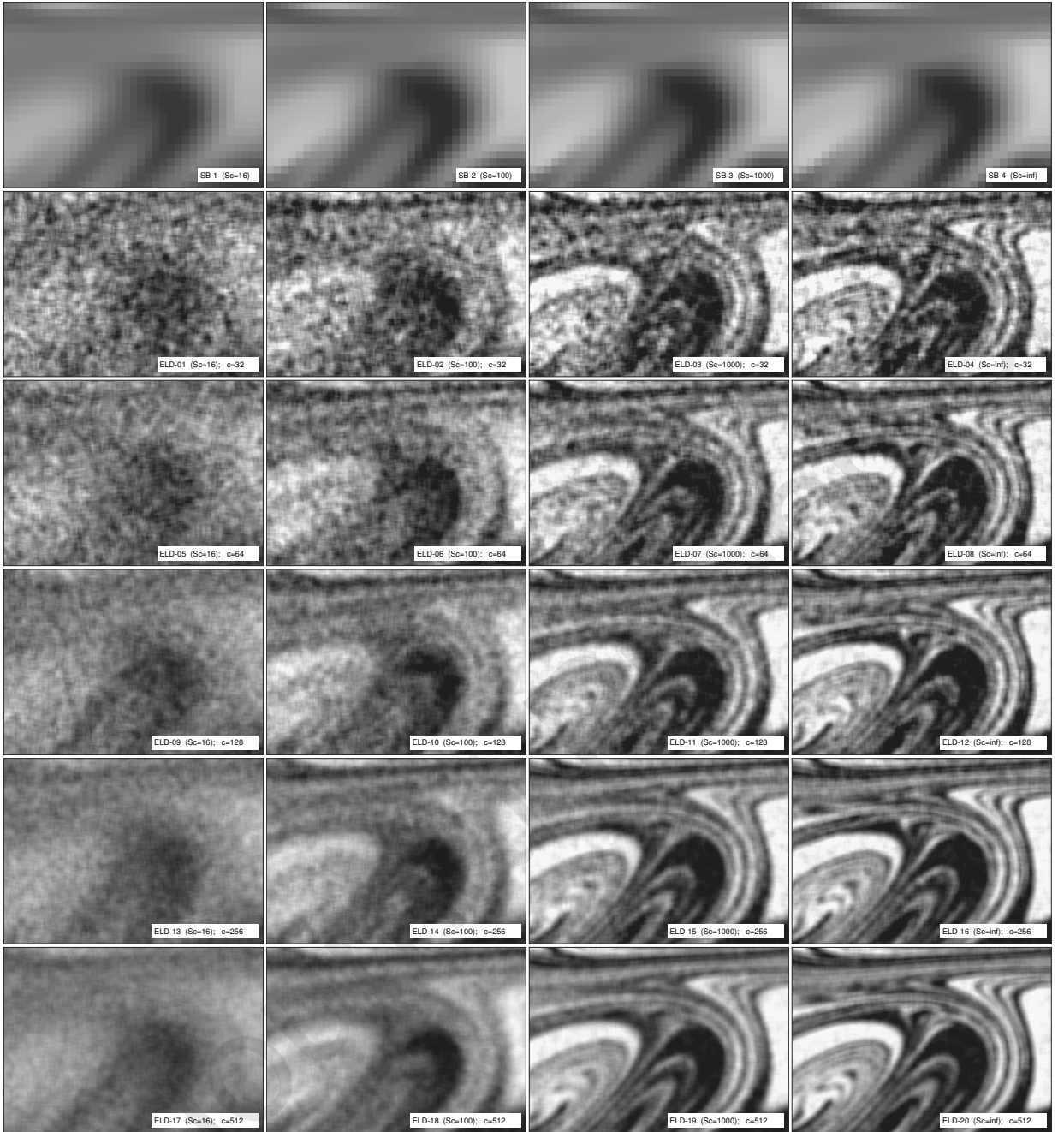


Fig. 16: A 2-dimensional slice of the size  $35 \times 25$  FVM cells, of the scalar field at time-step 2000. From top to bottom: SUPERBEE references and results for ELD simulations with ascending ELD-constants. From left to right: Schmidt numbers are 16, 100, 1000 and infinity. For the ELD-reconstructions the order  $f = 8$  is applied. Grey-scaled colour-map reaches from 0 (dark) to 1 (light)

SUPERBEE simulations or the ELD simulations<sup>3</sup>. The ratio between the most expensive ELD simulation and the cheapest FVM simulation is 22.

Figure 18 shows the total number of particles and the number of added particles due to re-initialisation events

<sup>3</sup>A high Schmidt number, however, makes a high ELD constant advantageous and thus yields higher computational costs nonetheless, as was pointed out in the previous sections

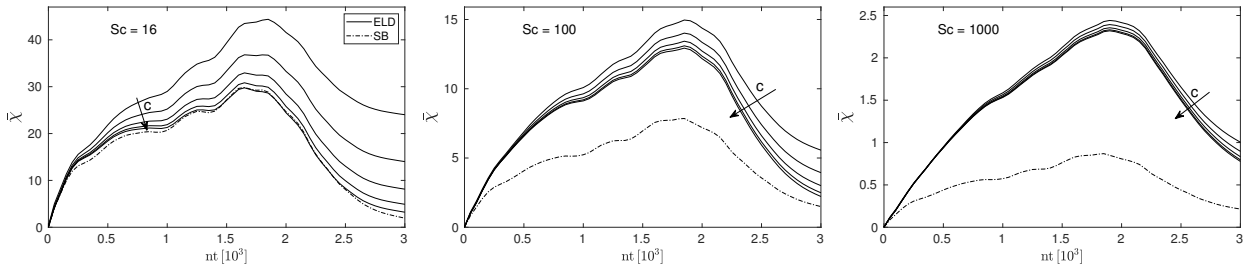


Fig. 17: Field-averaged scalar dissipation rates over simulation course for all cases with  $Sc = 16$  (left),  $Sc = 100$  (middle) and  $Sc = 1000$  (right).

| Case   | $c$ | $Sc$ | Computation time<br>[hh:mm:ss] | Cost<br>[CPUh] | Max. particle<br>count [mio.] |
|--------|-----|------|--------------------------------|----------------|-------------------------------|
| SB-1   | -   | 16   | 00:12:07                       | 436            | -                             |
| SB-2   | -   | 100  | 00:11:55                       | 429            | -                             |
| SB-3   | -   | 1000 | 00:12:02                       | 433            | -                             |
| SB-4   | -   | inf  | 00:11:44                       | 422            | -                             |
| ELD-1  | 32  | 16   | 00:31:45                       | 1143           | 230                           |
| ELD-2  | 32  | 100  | 00:30:53                       | 1112           | 257                           |
| ELD-3  | 32  | 1000 | 00:31:22                       | 1129           | 262                           |
| ELD-4  | 32  | inf  | 00:31:35                       | 1137           | 263                           |
| ELD-5  | 64  | 16   | 00:40:55                       | 1473           | 514                           |
| ELD-6  | 64  | 100  | 00:39:04                       | 1406           | 567                           |
| ELD-7  | 64  | 1000 | 00:40:56                       | 1474           | 578                           |
| ELD-8  | 64  | inf  | 00:43:55                       | 1581           | 579                           |
| ELD-9  | 128 | 16   | 00:55:39                       | 2003           | 1095                          |
| ELD-10 | 128 | 100  | 00:57:28                       | 2069           | 1205                          |
| ELD-11 | 128 | 1000 | 01:01:45                       | 2223           | 1226                          |
| ELD-12 | 128 | inf  | 00:57:55                       | 2085           | 1229                          |
| ELD-13 | 256 | 16   | 01:38:47                       | 3556           | 2266                          |
| ELD-14 | 256 | 100  | 01:45:20                       | 3792           | 2485                          |
| ELD-15 | 256 | 1000 | 01:41:56                       | 3670           | 2527                          |
| ELD-16 | 256 | inf  | 01:39:33                       | 3584           | 2532                          |
| ELD-17 | 512 | 16   | 04:09:04                       | 8966           | 4652                          |
| ELD-18 | 512 | 100  | 04:15:23                       | 9194           | 5095                          |
| ELD-19 | 512 | 1000 | 04:18:38                       | 9311           | 5180                          |
| ELD-20 | 512 | inf  | 04:13:36                       | 9130           | 5190                          |

Table 3: Statistics regarding the computational cost for the 24 test cases.

for three ELD-simulations with different ELD-constants over simulation time. The change in the total number of particles over time and the addition of new particles per time step are proportional to each other depending on the ELD-constant. The amount of added particles increases rapidly at the beginning of the simulation while the mixing layer forms and expands. It then remains almost constant and decreases steadily from about time step 2000 on. The decrease in the amount of added particles per time step can be attributed to both, decaying turbulence and mixing progress, both leading to a decrease in gradients and scalar variance production rates. Being the time integral of the particle addition, the total number of particles corresponds to a degressive course.

Due to the flow geometry of the mixing layer, the number of particles is not evenly distributed over the entire

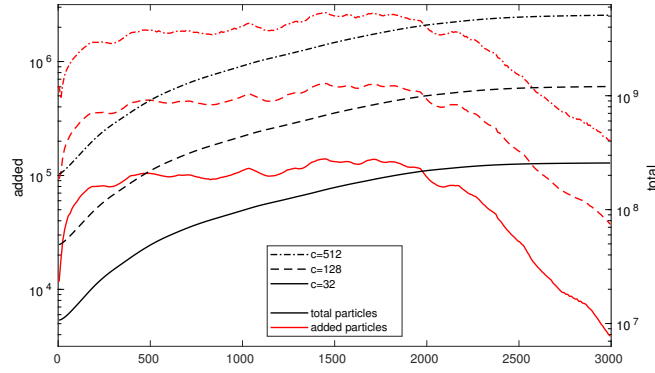


Fig. 18: Total number of particles and added particles by re-initialisation for three ELD-simulations with  $Sc = 1000$  and different ELD-constants  $c = 32$ ,  $c = 128$  and  $c = 512$ , respectively

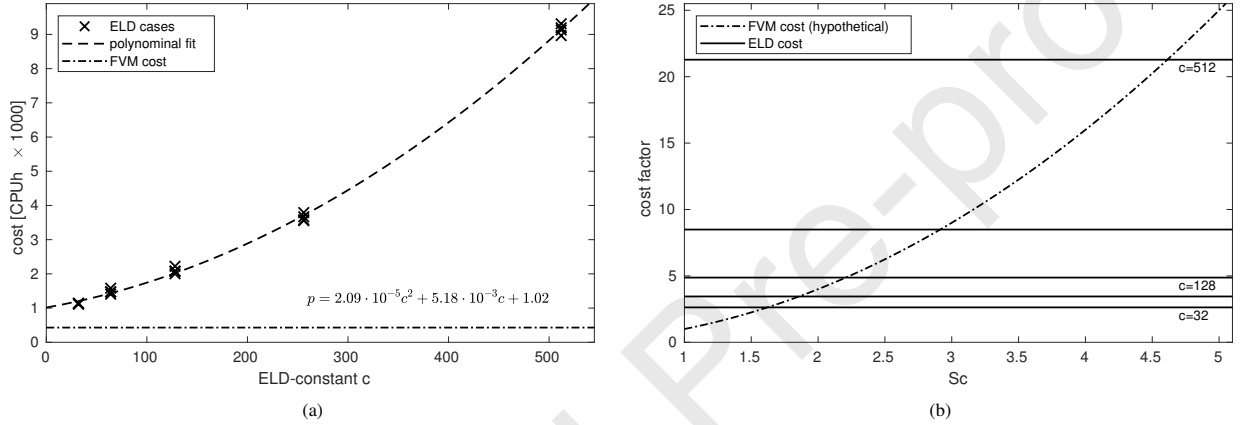


Fig. 19: Figure (a) shows the computational cost of the 20 ELD-cases over their ELD-constant and a second order polynomial fit of the data. The dash-dotted line refers to the cost of the reference SUPERBEE simulations. In Figure (b) the dash-dotted line expresses the hypothetical factor, by which the cost of an FVM simulation increases for raising Schmidt-numbers. The solid lines represent the cost factor of different ELD-constants ( $c = \{32, 64, 128, 256, 512\}$ ) compared with the baseline FVM simulation at  $Sc = 1$ . The values are taken from averaging the statistics in table 3 regarding the respective value for  $c$

domain. At  $Sc = 1000$  and  $c = 512$  (test case ELD-19) for instance, the most sparsely populated sub-domain contains 45 particles at time step 1500, while the most densely populated one contains 2.8 million particles. As the mixing layer develops and expands over an increasing proportion of the domain, this imbalance decreases. During time step 3000, for the same test case, the most sparsely populated sub-domain contains 2.0 million particles, while the most densely populated sub-domain contains 2.6 million particles. As a result, the speed at which the simulation is executed is limited by the sub-domain with the highest number of particles.

As Fig. 19 (a) shows, the dependence of computational costs on the ELD-constant can be accurately approximated by a second-order polynomial. The correlation is slightly over-proportional, since the threshold for creating new particles decreases with a higher ELD constant and thus an over-proportional number of particles are created, especially for the reproduction of very fine structures. With this dependence, the computational cost of an ELD-method can be estimated a priori. It is difficult to compare the cost of an ELD simulation with an equivalent SUPERBEE FVM simulation in terms of high Schmidt numbers. Due to the small Batchelor scale, the FVM simulation would have to be extremely finely resolved, which is hardly feasible. The factor by which the cost of a resolved FVM simulation scales with increasing Schmidt numbers can be estimated very hypothetically with eq. 2. With a quadrupling of the Schmidt number, the grid resolution must accordingly be doubled in each spatial direction, whereby the time step in an explicit simulation needs to be halved due to the CFL condition. The cost therefore scales with:  $\text{costfactor} = (Sc^{0.5})^4 = Sc^2$ . However, such an estimate is very hypothetical and subject to strict reservations, as many influencing factors are ignored. Fig. 19 (b) shows the evolution of the cost factor for an FVM simulation according to this simple estimation, with the grid resolution adjusted according to the changing Batchelor scale. In addition, the mean cost factors of the

ELD simulations compared to the baseline FVM simulation are determined from table 3 and plotted. Each intersection of an ELD cost factor with the hypothetical FVM cost curve represents a break-even point at which the corresponding ELD simulation is potentially more favourable than a classical FVM simulation in terms of computational cost only.

## 5. Conclusions

The presented ELD-method continues efforts to provide efficient numerical techniques that address the multi-scale behaviour of turbulent scalar transport, especially at high Schmidt numbers. Similar to established concepts, such as the Lagrangian PDF methods, it is based on the idea of combining the numerical efficiency made possible by the Eulerian description with the numerical stability provided by the Lagrangian description. The novelty lies in the conservative, constantly self-re-initialising decomposition of a scalar field into a low-frequency "smooth" component, which is transported by the finite volume method with negligible numerical diffusion or oscillation and a high-frequency "fine-structured" component, which is transported by particles. As a significant advance, this decomposition allows a concentrated use of particles in regions where they provide a substantial gain in resolution. It has been shown that the ELD method is able to significantly reduce the numerical diffusion in comparison to FVM simulations that use the SUPERBEE TVD delimiter. At the same time, it was possible to reconstruct very detailed information from the particle data, which by far exceeds the resolution of the grid. The extraction of this information also proved the physically meaningful transport of small scales. For a quantitative assessment, however, this study should be followed by a validation of the ELD method through a comparison with numerically simulated or experimentally determined flows with high Schmidt numbers.

As expected, the computational costs of this method are increased due to the high Lagrangian particle concentrations. However, these costs are small compared to the potential costs that alternative high-resolution FVM simulations would bring. At this stage, the ELD method has elementary disadvantages compared to classical FVM simulations with typical scalar transport schemes like TVD. Particularly with low ELD-constants, noise arises during the reconstruction of an Eulerian field from the particle data. This noise makes the method prone to unboundedness and it reduces the benefit of the method especially for small Schmidt numbers. Apart from validation, future work should aim to eliminate or at least control these problems at low ELD-constants. Likewise, the study of the individual parameters, foremost the ELD-constant, and the filter width should be intensified. In this regard, the localised diffusion filter introduced by this study should be investigated in detail and its effect quantified in comparison to the use of a generic Gaussian filter. At the same time, other schemes for the convective transport of the Eulerian low-frequency component should be tested or specially adapted ones should be developed. This would allow the filter threshold to be raised and less scalar mass would have to be deposited into the high-frequency component. This would result in a lower particle concentration and thus a higher numerical efficiency. The value of the method at low Schmidt numbers could be improved by removing the noise through appropriate filtering. Thus, an efficient method with little numerical diffusivity could also be provided for this range of application. For the re-initialisation step, in addition to adding new particles, it should be considered to remove existing ones at points where the scalar field has already become smooth by itself due to physical diffusion, in order to further increase numerical efficiency.

Future work should also consider and explore the method in the context of LES since the fine reconstruction properties of the ELD method suggest that mixing scales can be resolved which are significantly finer than the LES resolution. This will require to incorporate the sub-grid-scale eddy viscosity into the particle motion equation (21) and to find an accurate calibration of this formulation.

## Acknowledgments

The authors gratefully acknowledge the computing time granted by the Center for Computational Sciences and Simulation (CCSS) of the University of Duisburg-Essen on the supercomputer magnitUDE (DFG grant INST 20876/209-1 FUGG, INST 20876/243-1) at the Zentrum für Informations- und Mediendienste (ZIM).

## Appendix A. An investigation on the filter width

Being a key ELD parameter, the filter width  $\sigma_f$  is examined in the following. A mixing layer setup is chosen analogous to section 3, whereby the domain size is slightly reduced in terms of both physical and logical extent. The initial conditions are again set so that the Kolmogorov length scale corresponds approximately to twice the



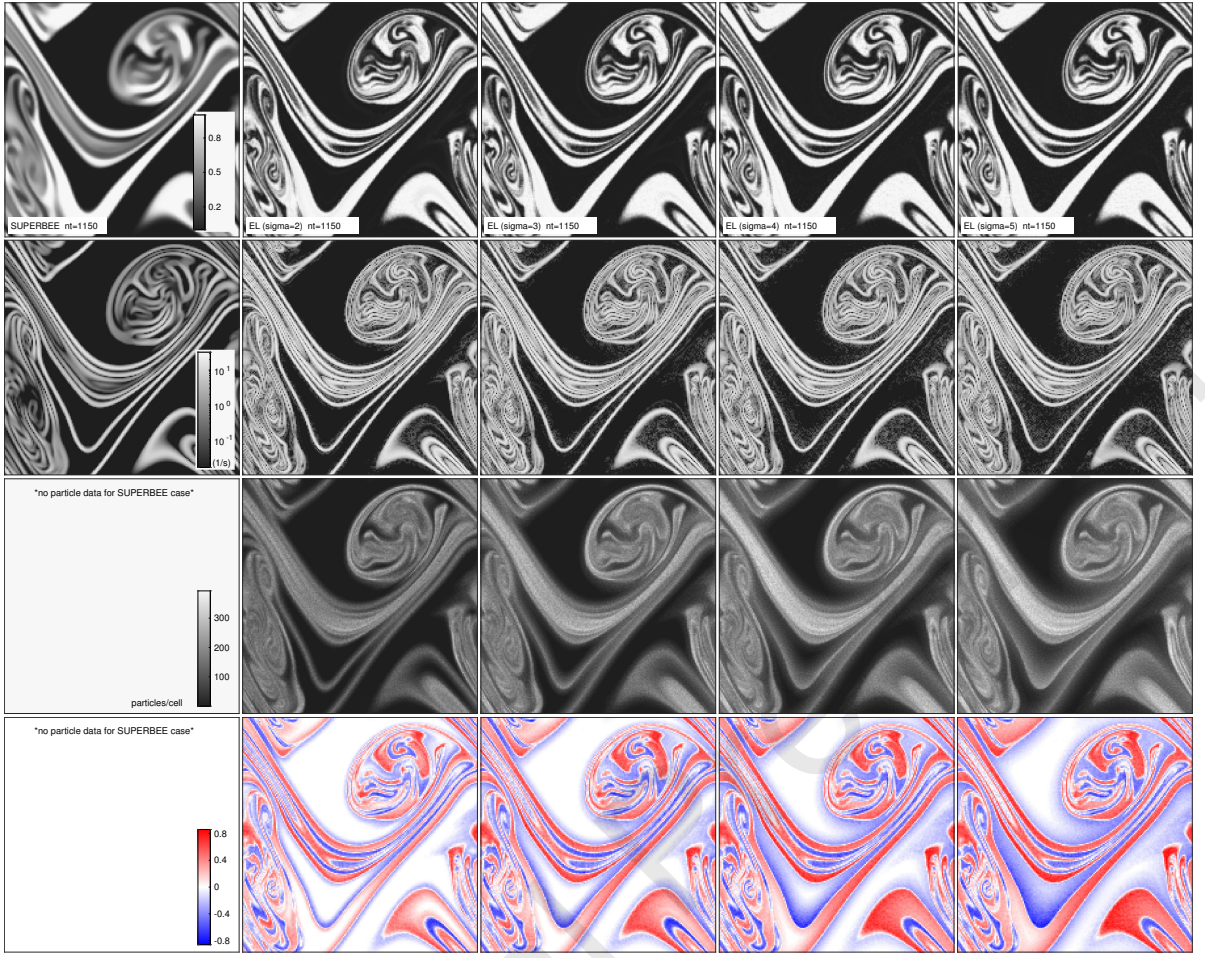


Fig. 20: Visualisation of the influence of the filter width  $\sigma_f$ . From top to bottom: Total scalar field  $\Phi$ , scalar dissipation  $\chi$ , Lagrangian particle concentration and high-frequency field  $\Phi_L$ . From left to right: SUPERBEE reference simulation followed by ELD-simulations with  $\sigma_f = 2$ ,  $\sigma_f = 3$ ,  $\sigma_f = 4$ , and  $\sigma_f = 5$

grid spacing. For the filter width  $\sigma_f$  the following values are set in sequence and simulated with the ELD method:  $\sigma_f = \{2, 3, 4, 5\}$ . The Schmidt number is set to  $Sc = 100$  and the ELD-constant to  $c = 100$ . In addition, a classic FVM simulation with TVD and SUPERBEE delimiter is carried out as a reference. Fig 20 shows the results in terms of the scalar field, the scalar dissipation and the particle concentration, comparing the different filter widths with each other. A distinct correlation between the scalar dissipation and the particle concentration can be observed. Particles occur exactly where the scalar variance dissipates. The particles are only required locally, while much of the domain is free of particles. The filter width influences whether the particles are more localised and more centred, or whether they are distributed more widely over the scalar discontinuity. At a filter width of  $\sigma_f = 2$ , the scalar dissipation and the particle concentration appear to be in the best qualitative agreement. The high-frequency fields explain, how a structured and textured scalar dissipation field can emerge from a fairly smooth particle concentration field due to the interaction of positive and negative particles.

The influence of the filter width on the scalar RMS and thus the unmixedness as well as on the computational cost is examined. Fig 21 shows the temporal course of the RMS as well as the total particle number. The RMS increases with higher filter width. The curves for  $\sigma_f = 4$  and  $\sigma_f = 5$  are almost on line, the RMS seems to have converged there with respect to  $\sigma_f$ . The total number of particles and thus the computational cost increases only slightly with increasing filter width. For the tests in this paper, the value  $\sigma_f = 4$  is adopted as the filter width because of the apparent convergence with respect to the RMS and because the impact on the computational cost is moderate.

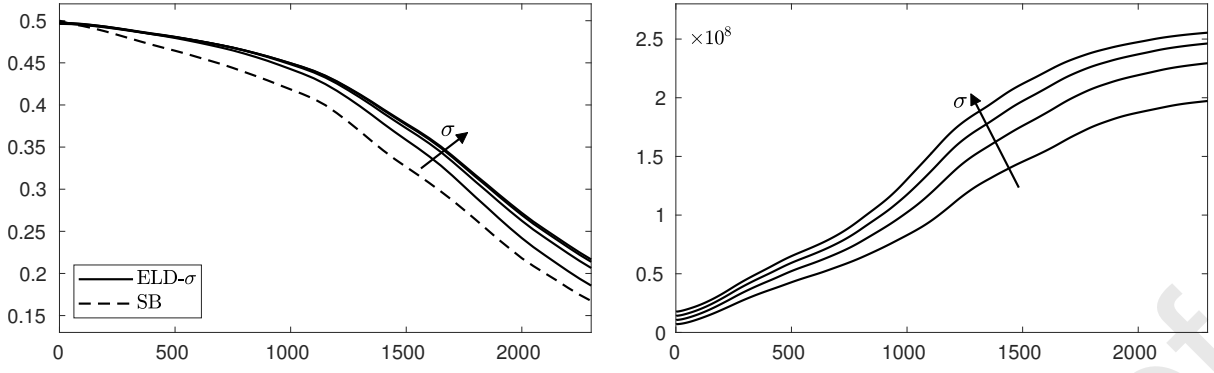


Fig. 21: Scalar RMS over simulation time for different filter widths ( $\sigma_f = \{2, 3, 4, 5\}$ ) and SUPERBEE reference on the left. Total particle count over simulation time for the corresponding filter widths on the right

## Appendix B. Details on the turbulent flow field

The main purpose of the method is to represent and transport scalar structures that are far below the FVM resolution. In terms of the particle motion equation eq. (21) and apart from the chosen ELD-constant  $c$ , the scalar convection accuracy is linked to the velocity field accuracy. For an ideal scalar convection, combining these considerations, all scales of momentum are to be completely resolved, while the smallest mixing scales should stay well below the cell-size  $\Delta$ , considering a high Schmidt number. Therefore it is evident that the initial velocity  $U_0$  and the physical domain size are to be selected such that the expected Kolmogorov scale  $\eta_K$  is related to  $\Delta$ , while the Batchelor scale  $\eta_B$  is under-resolved. Following the advise of Moin and Mahesh [56], the grid resolution should be in the order of the Kolmogorov length scale for this purpose but not necessarily below. In line with a conservative attitude, a Kolmogorov length scale corresponding to twice the grid spacing is targeted. To reach this, the optimal starting conditions were estimated analytically by using an approach related to Prandtl's mixing-length concept [57]. Then, in the post-processing, the dissipation rate is computed from the flow field and the Kolmogorov scale is validated.

According to the analytical estimation, the initial bulk velocity is set to  $U_0 = 3.0 \text{ m s}^{-1}$  and the physical domain extent to  $D_x = D_y = D_z = 6 \text{ mm}$ . At the post-processing of a test run, the smallest momentum scales are then verified based on the procedure by Rieth et al. [49]. The turbulence can be expected homogeneous in x- and z- direction. Spatial averaging in these directions yields statistical mean quantities  $\bar{\Phi}(y, t)$ ,

$$\bar{\Phi}(y, t) = \frac{1}{D_x D_z} \int_0^{D_z} \int_0^{D_x} \Phi(x, y, z, t) dx dz. \quad (27)$$

With this relationship local velocity fluctuations can be calculated as  $u'_i = u_i - \bar{u}$ . Following this, the mean dissipation rate can be computed as a function of time and the vertical coordinate  $y$ ,

$$\epsilon(y, t) = \frac{1}{\rho} \overline{\tau_{ij} \frac{\partial u'_i}{\partial x_j}}. \quad (28)$$

Subsequently the Kolmogorov scale can also be evaluated as a function of time and the vertical coordinate,

$$\eta_K(y, t) = \left( \frac{\nu^3}{\epsilon} \right)^{1/4}. \quad (29)$$

From the simulated flow field, the turbulence Reynolds number is calculated as  $\text{Re}_T = k^{1/2} L / \nu$  where the turbulence kinetic energy is  $k = (u_i - \bar{u}_i)^2 / 2$ , and the turbulence length scale is given by  $L = k^{3/2} / \epsilon$ . Figure 22 shows the averaged Kolmogorov length scale and the averaged turbulent Reynolds number over time, obtained by the aforementioned procedure.

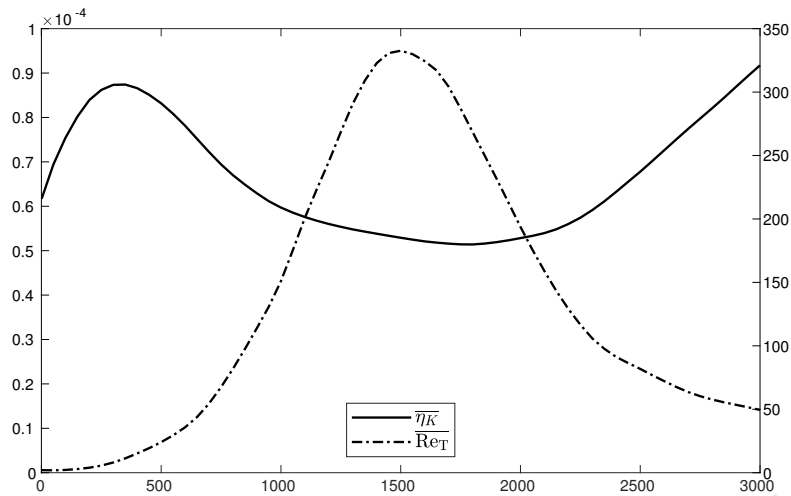


Fig. 22: Domain-averaged Kolmogorov length scale  $\overline{\eta_K}$  and turbulent Reynolds number  $\overline{Re_T}$  over simulation time.

## References

- [1] A. Kolmogorov, The local structure of isotropic turbulence in an incompressible viscous fluid, in: Dokl. Akad. Nauk SSSR, volume 30, 1941, pp. 301–305.
- [2] G. K. Batchelor, Small-scale variation of convected quantities like temperature in turbulent fluid part 1. general discussion and the case of small conductivity, *Journal of Fluid Mechanics* 5 (1959) 113–133.
- [3] P. E. Dimotakis, Turbulent mixing, *Annual Review of Fluid Mechanics* 37 (2005) 329–356.
- [4] D. A. Donzis, K. Sreenivasan, P. Yeung, The batchelor spectrum for mixing of passive scalars in isotropic turbulence, *Flow, turbulence and combustion* 85 (2010) 549–566.
- [5] D. Donzis, P. Yeung, Resolution effects and scaling in numerical simulations of passive scalar mixing in turbulence, *Physica D: Nonlinear Phenomena* 239 (2010) 1278–1287.
- [6] A. Alexakis, L. Biferale, Cascades and transitions in turbulent flows, *Physics Reports* 767 (2018) 1–101.
- [7] K. R. Sreenivasan, Turbulent mixing: A perspective, *Proceedings of the National Academy of Sciences* 116 (2019) 18175–18183.
- [8] B. E. Rapp, *Microfluidics: modeling, mechanics and mathematics*, William Andrew, 2016.
- [9] N. Branley, W. Jones, Large eddy simulation of a turbulent non-premixed flame, *Combustion and flame* 127 (2001) 1914–1934.
- [10] H. Pitsch, H. Steiner, Large-eddy simulation of a turbulent piloted methane/air diffusion flame (sandia flame d), *Physics of fluids* 12 (2000) 2541–2554.
- [11] A. Kempf, R. Lindstedt, J. Janicka, Large-eddy simulation of a bluff-body stabilized nonpremixed flame, *Combustion and flame* 144 (2006) 170–189.
- [12] D. Deglon, C. Meyer, Cfd modelling of stirred tanks: Numerical considerations, *Minerals Engineering* 19 (2006) 1059–1068.
- [13] F. Zhang, S. Marre, A. Erriguible, Mixing intensification under turbulent conditions in a high pressure microreactor, *Chemical Engineering Journal* 382 (2020) 122859.
- [14] P. Rodrigues, B. Franzelli, R. Vicquelin, O. Gicquel, N. Darabiha, Coupling an les approach and a soot sectional model for the study of sooting turbulent non-premixed flames, *Combustion and Flame* 190 (2018) 477–499.
- [15] M. E. Mueller, H. Pitsch, Les model for sooting turbulent nonpremixed flames, *Combustion and Flame* 159 (2012) 2166–2180.
- [16] F. Bisetti, G. Blanquart, M. E. Mueller, H. Pitsch, On the formation and early evolution of soot in turbulent nonpremixed flames, *Combustion and Flame* 159 (2012) 317–335.
- [17] F. Harlow, Pic method for fluid dynamics calculations, Technical Report, Los Alamos Scientific Lab., N. Mex., 1961.
- [18] F. H. Harlow, The particle-in-cell method for numerical solution of problems in fluid dynamics, Technical Report, Los Alamos Scientific Lab., N. Mex., 1962.
- [19] F. H. Harlow, The particle-in-cell computing method for fluid dynamics, *Methods Comput. Phys.* 3 (1964) 319–343.
- [20] F. H. Harlow, Pic and its progeny, *Computer Physics Communications* 48 (1988) 1–10.
- [21] F. H. Harlow, J. E. Welch, Numerical calculation of time-dependent viscous incompressible flow of fluid with free surface, *The physics of fluids* 8 (1965) 2182–2189.
- [22] J. Welch, F. Harlow, J. Shannon, B. Daly, The mac method, los alamos scientific lab, Report LA-3425, Los Alamos, New Mexico (1966).
- [23] S. McKee, M. Tomé, J. Cuminato, A. Castelo, V. Ferreira, Recent advances in the marker and cell method, *Archives of Computational Methods in Engineering* 11 (2004) 107.
- [24] Y. Zhu, R. Bridson, Animating sand as a fluid, *ACM Transactions on Graphics (TOG)* 24 (2005) 965–972.
- [25] C. Fu, Q. Guo, T. Gast, C. Jiang, J. Teran, A polynomial particle-in-cell method, *ACM Transactions on Graphics (TOG)* 36 (2017) 1–12.
- [26] S. Pope, Lagrangian pdf methods for turbulent flows, *Annual review of fluid mechanics* 26 (1994) 23–63.
- [27] R. Lindstedt, S. Louloudi, E. Váos, Joint scalar probability density function modeling of pollutant formation in piloted turbulent jet diffusion flames with comprehensive chemistry, *Proceedings of the Combustion Institute* 28 (2000) 149–156.
- [28] R. P. Lindstedt, S. A. Louloudi, Joint-scalar transported pdf modeling of soot formation and oxidation, *Proceedings of the Combustion Institute* 30 (2005) 775–783.

- [29] W. Jones, S. Navarro-Martinez, Numerical study of n-heptane auto-ignition using les-pdf methods, *Flow, turbulence and combustion* 83 (2009) 407–423.
- [30] S. Viswanathan, H. Wang, S. B. Pope, Numerical implementation of mixing and molecular transport in les/pdf studies of turbulent reacting flows, *Journal of Computational Physics* 230 (2011) 6916–6957.
- [31] D. Enright, R. Fedkiw, J. Ferziger, I. Mitchell, A hybrid particle level set method for improved interface capturing, *Journal of Computational Physics* 183 (2002) 83–116.
- [32] S. Osher, J. A. Sethian, Fronts propagating with curvature-dependent speed: Algorithms based on hamilton-jacobi formulations, *Journal of computational physics* 79 (1988) 12–49.
- [33] J. A. Sethian, Evolution, implementation, and application of level set and fast marching methods for advancing fronts, *Journal of computational physics* 169 (2001) 503–555.
- [34] S. Osher, R. Fedkiw, Level set methods and dynamic implicit surfaces, volume 153, Springer Science & Business Media, 2006.
- [35] J.-B. Lagaert, G. Balarac, G.-H. Cottet, P. Bégou, Particle method: an efficient tool for direct numerical simulations of a high schmidt number passive scalar in turbulent flow, in: *Summer Program 2012. Center of Turbulence Research*, 2012, pp. 167–176.
- [36] G.-H. Cottet, G. Balarac, M. Coquerelle, Subgrid particle resolution for the turbulent transport of a passive scalar, in: *Advances in Turbulence XII*, Springer, 2009, pp. 779–782.
- [37] J.-B. Lagaert, G. Balarac, G.-H. Cottet, Hybrid spectral-particle method for the turbulent transport of a passive scalar, *Journal of Computational Physics* 260 (2014) 127–142.
- [38] S. Santoso, J.-B. Lagaert, G. Balarac, G.-H. Cottet, Hybrid particle-grid methods for the study of differential diffusion in turbulent flows, *Computers & Fluids* (2021) 105018.
- [39] R. Pohorecki, J. Baldyga, New model of micromixing in chemical reactors. 1. general development and application to a tubular reactor, *Industrial & engineering chemistry fundamentals* 22 (1983) 392–397.
- [40] J. Baldyga, Turbulent mixer model with application to homogeneous, instantaneous chemical reactions, *Chemical Engineering Science* 44 (1989) 1175–1182.
- [41] J. Baldyga, A closure model for homogeneous chemical reactions, *Chemical engineering science* 49 (1994) 1985–2003.
- [42] G. Zhou, L. Davidson, E. Olsson, Transonic inviscid/turbulent airfoil flow simulations using a pressure based method with high order schemes, in: *Fourteenth international conference on numerical methods in fluid dynamics*, Springer, 1995, pp. 372–378.
- [43] J. Williamson, Low-storage runge-kutta schemes, *Journal of Computational Physics* 35 (1980) 48–56.
- [44] S. B. Pope, *Turbulent flows*, 2001.
- [45] G. E. Box, A note on the generation of random normal deviates, *Ann. Math. Statist.* 29 (1958) 610–611.
- [46] A. Kempf, M. Klein, J. Janicka, Efficient generation of initial-and inflow-conditions for transient turbulent flows in arbitrary geometries, *Flow, Turbulence and combustion* 74 (2005) 67–84.
- [47] M. Klein, A. Sadiki, J. Janicka, A digital filter based generation of inflow data for spatially developing direct numerical or large eddy simulations, *Journal of computational Physics* 186 (2003) 652–665.
- [48] A. Kempf, S. Wysocki, M. Pettit, An efficient, parallel low-storage implementation of klein’s turbulence generator for les and dns, *Computers & fluids* 60 (2012) 58–60.
- [49] M. Rieth, A. Kempf, A. Kronenburg, O. Stein, Carrier-phase dns of pulverized coal particle ignition and volatile burning in a turbulent mixing layer, *Fuel* 212 (2018) 364–374.
- [50] K. Wan, L. Vervisch, Z. Gao, P. Domingo, C. Jiang, J. Xia, Z. Wang, Development of reduced and optimized reaction mechanism for potassium emissions during biomass combustion based on genetic algorithms, *Energy* 211 (2020) 118565.
- [51] A. Kempf, B. J. Geurts, J. Oefelein, Error analysis of large-eddy simulation of the turbulent non-premixed sydney bluff-body flame, *Combustion and flame* 158 (2011) 2408–2419.
- [52] F. Proch, P. Domingo, L. Vervisch, A. M. Kempf, Flame resolved simulation of a turbulent premixed bluff-body burner experiment. part i: Analysis of the reaction zone dynamics with tabulated chemistry, *Combustion and Flame* 180 (2017) 321–339.
- [53] P. L. Roe, Modelling of discontinuous flows, *Lectures in Applied Mathematics* 22 (1985).
- [54] E. Villermaux, Mixing and spray formation in coaxial jets, *Journal of propulsion and power* 14 (1998) 807–817.
- [55] E. Villermaux, H. Rehab, Mixing in coaxial jets, *Journal of Fluid Mechanics* 425 (2000) 161–185.
- [56] P. Moin, K. Mahesh, Direct numerical simulation: a tool in turbulence research, *Annual review of fluid mechanics* 30 (1998) 539–578.
- [57] L. Prandtl, Siebter bericht ueber untersuchungen zur ausgebildeten turbulenz, *ZAMM-Journal of Applied Mathematics and Mechanics* 5 (1925) 136–139.

**Declaration of interests**

☒ The authors declare that they have no known competing financial interests or personal relationships that could have appeared to influence the work reported in this paper.

☐ The authors declare the following financial interests/personal relationships which may be considered as potential competing interests:

|  |
|--|
|  |
|--|

## CRediT author statement

**M. Leer:** Methodology, Software, Investigation, Writing - Original Draft

**M. W. A. Pettit:** Methodology, Software, Investigation, Writing - Review & Editing **J. T. Lipkowitz:** Software, Supervision **P. Domingo:** Supervision,

Writing - Review & Editing **L. Vervisch:** Supervision, Methodology, Writing - Review & Editing **A. Kempf:** Conceptualisation, Methodology, Software,

Writing - Review & Editing, Supervision